# ANALYTICALLY DERIVING HOW RING LASER AND FIBER OPTIC GYROS MEASURE ANGULAR ROTATION

**Paul G. Savage**
Strapdown Associates, Inc.
Maple Plain, MN 55359 USA

WBN-14023
www.strapdowassociates.com
November 1, 2018 (Updated March 31, 2019)

ABSTRACT

This article provides a rigorous derivation of the analytics governing the operation of optical angular rotation sensors, ring laser gyros (RLGs) and fiber optic gyros (FOGs). Analytical predictions match known actual gyro test results, showing how angular rotation induces phase shift in oppositely directed monochromatic light waves traversing a closed waveguide, then measured by photo detectors for output. The waveguide is formed by reflecting mirrors in an RLG and by a fiber optic coil in a FOG. Classical Galilean/Newtonian kinematics explains how rotation affects each oppositely directed wave. When rotation induced tangential velocity of the waveguide is small compared to the speed of light, it is shown that Relativity theory predicts the same result. To analytically derive how the waves intersect in space-time when merged at the gyro readout, Relativity theory alone is required for the solution. The result is a single equation describing the net phase shift induced by rotation in the merged waves when illuminating the gyro readout photo detector. Applying the equation to an RLG shows how cyclic outputs are generated from the photo detector, each representing a known increment of angular rotation. Application to a FOG shows how successive angular rotation increments are measured, each over the time for a wave to traverse the fiber coil. Analysis of "closed-loop" FOG operations derives how to operate L/N (lithium–niobate) crystals inserted in the fiber coil to balance rotation induced phase shift and generate angular rotation outputs. Two closed-loop FOG configurations are analytically described, one using symmetrical dual L/N crystal inserts, the other using a single L/N crystal to reduce manufacturing cost. Included are methods for eliminating round-off error in FOG digital conversion operations.

## INTRODUCTION

Optical gyros (ring laser and fiber optic) have been in broad usage since the late 1970s. Curiously, however, their basic principle of operation has varied between designers and users. Optical gyros measure the change in phase induced by angular rotation in oppositely directed monochromatic light waves created within the gyro. Some attribute the phase change to Relativity theory while others characterize it as a classical kinematic Doppler effect. Many of these and other explanations have relied on intuitive reasoning to explain actually measured optical gyro operating characteristics. The purpose of this article is to provide a rigorous

comprehensive analytic derivation of equations governing the operating characteristics of optical gyros and in the process, identify those attributed to classical vector kinematics, and those uniquely contributed by Relativity. The analysis is based on idealized optical gyro configurations in which the oppositely directed light waves are independent from one-another, unaffected by imperfections in the closed waveguide directing their motion within the gyro, and having the same polarization direction when combined at the readout photo detector.

Relativity theory relates the motion of a point in space as measured by two remote observers in motion relative to one-another. When the velocity magnitude between observers is small compared to the speed of light, the observed motion forecasted by Special Relativity theory [1 Part 1; 2 Chpt VI; 3] reduces to classical Galilean kinematic predictions [1 pp 37-38; 2 Chpt III Sect 7; 4 Sect 12-1]. Such is the case for optical gyros when analyzing how angular rotation impacts each of two oppositely directed light waves travelling within the gyro along a common closed optical path. Similar to the Doppler-like frequency shift observed in light waves emanating from receding stars, both Galilean and relativistic kinematics predict an angular rotation induced wavelength shift in the optical gyro light waves, increasing for the wave travelling in the direction of rotation, decreasing for the oppositely directed wave. Coupled with the shift in wavelength, Relativity predicts that the speed of propagation for each of the oppositely directed light waves will be the same "speed-of-light" relative to the rotating waveguide, as it is for light waves propagating through non-rotating inertial space. The light wave frequencies equate to the speed-of-light constant divided by the wavelength, thus, decrease for waves travelling with the rotation and conversely for the oppositely directed waves, generating a frequency difference between the oppositely directed waves. When the oppositely directed waves are mixed by the gyro readout, a combined beam power signal is generated whose intensity measures the rotation induced frequency difference. The combined beam power illuminates a readout photo detector, thereby generating a measurement of angular rotation. This is exactly what is produced in operating optical gyros under rotation, and what is predicted by the analytical development in this article.

Beginning from classical vector geometry, the article first describes the relationship between the position vector measured by each of two observers to the same remote point in space. Classical Newtonian differential kinematics then describes how the geometrical relationship changes due to differential motion of the remote point and between the observers while making observations. The equivalent result is also derived based on Special Relativity, producing the same Galilean/Newtonian derived result when the relative velocity magnitude between observers is small compared to the speed of light.

Both the Galilean/Newtonian and Relativity results are derived in non-rotating coordinates. The article then derives the equivalent in rotating coordinates by projecting the relative position vector geometry onto two non-rotating coordinate frames, one rotated from the other by a small angular rotation. The difference between the two projections is identified as the change that would be measured in a rotating coordinate frame undergoing the small angular rotation. Taken in the limit and substituting the original non-rotating coordinate result, derives an equation relating the differential motion of the remote point as measured by one observer in non-rotating coordinates, in terms of the differential measurement taken by the other observer in rotating coordinates.

The analytical development to this point in the article is general in nature. Continued analysis specializes the two observation points to be fixed within a rigid body (a gyro), defining the observed point in motion to be a photon of light traversing a waveguide within the gyro, defining one of the observation points to be in the waveguide at the start of a photon's differential motion, the other observation point at a reference "rotation center" external to the waveguide, and gyro rotation equated to that of the rotating coordinate frame. In the process, the photon in motion is defined to be part of a travelling light wave whose wavelength relative to the rotating gyro is a function of the wavelength in non-rotating space, the distance from the reference point to the photon, and the gyro's angular rotation during the time the photon traverses a wavelength of distance. The wavelength solution is then used to obtain independent integral solutions for each of the oppositely directed light waves traversing the gyro waveguide.

Analyses thus far in the article are performed using Galilean/Newtonian kinematics. (Appendix A demonstrates that Relativity theory obtains the same result when the velocity of the waveguide around the rotation center is small relative to the speed of light.) Combining the individual gyro light wave solutions in the readout zone at the same instant of time then requires application of Relativity theory. The method is to first recognize that in a non-rotating frame, the wave propagation speed at any point in the waveguide will be the same speed-of-light constant as it is open-space. Second, for the observer stationed in the rotating waveguide, the differential movement of a passing photon, although differentially rotated, will (to first order in differential rotation) be of the same magnitude as when measured in a non-rotating frame at the same location. By joining these observations, it is analytically shown that relative to the rotating waveguide, the propagation rate for each of the oppositely directed beams will be at the same speed-of-light, hence, the time interval for each wave to traverse a given distance relative to the waveguide will also be the same. Applying this finding to each of oppositely directed wave solutions allows them to be analytically summed into a single combined beam wave equation defining the beam power that will illuminate the gyro readout photo detector(s). The result equates the cumulative difference in phase between the individual waves to the integrated effect of angular rotation over a selected time interval. For the remainder of the article, the combined beam power equation is used to explain the operating characteristics of fiber optic and ring laser optical gyros.

Two types of ring laser gyro configurations are described, those in which the closed waveguide is constrained by reflecting mirror geometry to lie within a plane, and those in which the mirrors are angularly oriented to create a closed out-of-plane waveguide geometry. The results for each analytically demonstrates how combining the oppositely directed waves at the gyro readout creates an optical interference pattern that moves across the photo detector(s) at the angular rotation rate, generating cyclic outputs, each representing a known increment of angular rotation.

The combined beam power equation is then used to analytically describe two types of fiber optic gyros, those classified as "open-loop" and those classified as "closed-loop". Based on employing lithium-niobate (L/N) integrated-optics inserts in the fiber coil for injecting phase bias into the light waves, the closed-loop configuration adds control bias to the phase induced by angular rotation in the oppositely directed light beams. Using outputs from the gyro photo detector, L/N bias command equations are derived to balance the rotation induced phase

difference in the light waves, while simultaneously generating successive outputs of gyro angular rotation over the time for a light wave to traverse the fiber coil. Included in the L/N bias equations are provisions to eliminate round-off error in the three closed-loop electronics interface operations; 1) Digitally sampling photo detector analog measurements into the digital control loop processor, 2) Creating L/N analog bias control voltages from the digital control-loop processor, and 3) Converting angular rotation increments calculated in the control-loop processor for digital output format compatibility.

## NOTATION

The following general notation is used in the article:

$\underline{V}$ = Vector parameter having length and direction. Vectors in this article are classified as "free vectors" having no preferred location in coordinate frames in which they are analytically described.

$/ i$ = Subscript denoting the vector parameter being observed (measured or calculated from measurements) at observation point $i$ ($i$ being point $a$ or $b$).

Observable Event – An event at a position location in space at a particular instant in time (e.g., a lightning strike, explosion, illumination by a radar pulse, or passage of the leading edge of a light wave across a point in space) that can be observed at a remote spatial location based on electro-magnetic wave propagation (e.g. light or radar) [1 pp 29, 36; 2 pp 28, 236-238; 5 pp 10].

## DIFFERENTIAL POSITION MOTION IN NON-ROTATING COORDINATES

In non-rotating coordinates, Fig. 1 illustrates the geometrical relationship between distance vectors from two observation points $a$ and $b$ to a remote point $p$ at the same instant of time.

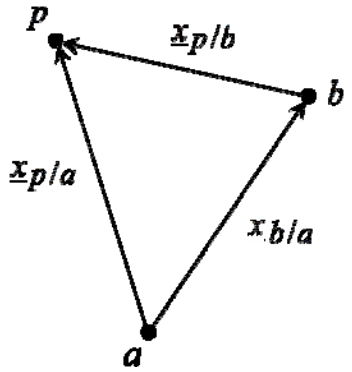


Fig. 1 – Position Vector Relationships At The Same Instant Of Time
In Non-Rotating Coordinates

In Fig. 1, $\underline{x}_{p/a}$ is the distance vector to point $p$ determined (observed) from point $a$, $\underline{x}_{p/b}$ is the distance vector to point $p$ observed from point $b$, and $\underline{x}_{b/a}$ is the distance vector to point $b$ determined from point $a$. At two successive time points $t_1$ and $t_2$ ($t_2$ following $t_1$), the kinematic representation in Fig. 1 can be described analytically by

$$\underline{x}_{p_1/a} = \underline{x}_{p_1/b} + \underline{x}_{b1/a} \qquad \underline{x}_{p_2/a} = \underline{x}_{p_2/b} + \underline{x}_{b2/a} \tag{1}$$

where subscripts 1 and 2 identify point locations at $t_1$ and $t_2$. The change in the Fig. 1 vector parameters between the $t_1$ and $t_2$ time instants is defined as

$$\Delta\underline{x}_{p/a} \equiv \underline{x}_{p_2/a} - \underline{x}_{p_1/a} \qquad \Delta\underline{x}_{p/b} \equiv \underline{x}_{p_2/b} - \underline{x}_{p_1/b} \qquad \Delta\underline{x}_{b/a} \equiv \underline{x}_{b_2/a} - \underline{x}_{b_1/a} \tag{2}$$

Taking the difference between the (1) equations and applying the (2) definitions finds

$$\Delta\underline{x}_{p/a} = \Delta\underline{x}_{p/b} + \Delta\underline{x}_{b/a} \tag{3}$$

IDENTIFYING COORDINATE FRAMES

Eqs. (1) – (3) are valid in any non-rotating coordinate frame. As in [6], let us now introduce non-rotating coordinate frames $B_1$ and $B_2$ defined as parallel to the instantaneous orientation of rotating coordinate frame $B$ at successive time instants $t_1$ and $t_2$. Because $B_1$ and $B_2$ are non-rotating relative to a common non-rotating space, the angular orientation of $B_2$ relative to $B_1$ will be constant. For clarity, the $\Delta\underline{x}_{p/b}$ and $\Delta\underline{x}_{b/a}$ definitions in (2) are now rewritten in $B_1$ coordinates as

$$\Delta\underline{x}^{B1}_{p/b} = \underline{x}^{B1}_{p_2/b} - \underline{x}^{B1}_{p_1/b} \tag{4}$$

$$\Delta\underline{x}^{B1}_{b/a} = \underline{x}^{B1}_{b2/a} - \underline{x}^{B1}_{b1/a} \tag{5}$$

where the $B_1$ superscript identifies the $B_1$ coordinate frame in which the vector components are projected (e.g., as elements of a column matrix).

The constituents of $\Delta\underline{x}^{B1}_{p/b}$ and $\Delta\underline{x}^{B1}_{b/a}$ in (4) and (5) can be related to distance vector measurements taken in $B_2$ coordinates coupled with the angular orientation relating the $B_1$ and $B_2$ coordinate frames:

$$\begin{aligned}
\Delta\underline{x}^{B1}_{p/b} &= \underline{x}^{B1}_{p_2/b} - \underline{x}^{B1}_{p_1/b} = C^{B1}_{B2}\,\underline{x}^{B2}_{p_2/b} - \underline{x}^{B1}_{p_1/b} = \left(C^{B1}_{B2} - I + I\right)\underline{x}^{B2}_{p_2/b} - \underline{x}^{B1}_{p_1/b} \\
&= \underline{x}^{B2}_{p_2/b} - \underline{x}^{B1}_{p_1/b} + \left(C^{B1}_{B2} - I\right)\underline{x}^{B2}_{p_2/b} \\
\Delta\underline{x}^{B1}_{b/a} &= \underline{x}^{B1}_{b_2/a} - \underline{x}^{B1}_{b_1/a} = C^{B1}_{B2}\,\underline{x}^{B2}_{b_2/a} - \underline{x}^{B1}_{b_1/a} = \left(C^{B1}_{B2} - I + I\right)\underline{x}^{B2}_{b_2/a} - \underline{x}^{B1}_{b_1/a} \\
&= \underline{x}^{B2}_{b_2/a} - \underline{x}^{B1}_{b_1/a} + \left(C^{B1}_{B2} - I\right)\underline{x}^{B2}_{b_2/a}
\end{aligned} \tag{6}$$

where superscript $B_2$ identifies vector component projections on $B_2$ coordinate axes, $I$ is the identity matrix, and $C^{B1}_{B2}$ is a direction cosine matrix that transforms vector components from their values in non-rotating (inertial) coordinates $B_2$ to their values in inertial coordinates $B_1$.

Since non-rotating frames $B_1$ and $B_2$ are defined as aligned with the rotating $B$ frame at time instants 1 and 2, we can calculate the change in $B$ frame values of a vector during the $t_1$ to $t_2$ time interval as the difference between the $B_1$ and $B_2$ projected values. Thus, for particular terms in (6),

$$\underline{x}^{B2}_{p_2/b} - \underline{x}^{B1}_{p_1/b} \equiv \Delta\underline{\chi}^{B}_{p/b} \qquad \underline{x}^{B2}_{b_2/a} - \underline{x}^{B1}_{b_1/a} \equiv \Delta\underline{\chi}^{B}_{b/a} \tag{7}$$

where from $t_1$ to $t_2$, $\Delta\underline{\chi}^{B}_{p/b}$ is the change in the distance vector from observation point $b$ to point $p$ in the rotating $B$ frame (superscript), and $\Delta\underline{\chi}^{B}_{b/a}$ is the change in the distance vector from observation point $a$ to point $b$ as measured at point $a$ in the rotating $B$ frame. We also note that $C^{B1}_{B2} - I$ in (6) represents the change in the $C^{B1}_{B}$ direction cosine matrix from its identity value at $t_1$ (when $B = B_1$) to its $C^{B1}_{B2}$ value at $t_2$. For the angular rotation over $t_1$ to $t_2$, $C^{B1}_{B2} - I$ can be equated to the equivalent rotation angle vector $\Delta\underline{\theta}^{B}_{IB}$ which for small angular rotation approximates as in [7 Sect 3.5.2 ]

$$C^{B1}_{B2} - I \approx \left(\Delta\underline{\theta}^{B}_{IB}\times\right) \tag{8}$$

where the $IB$ subscript indicates the angular rotation of frame $B$ from its orientation parallel to non-rotating inertial frame $B_1$ to its orientation parallel to non-rotating inertial frame $B_2$. Substituting (7) and (8) in (6) obtains

$$\Delta\underline{x}^{B1}_{p/b} = \Delta\underline{\chi}^{B}_{p/b} + \Delta\underline{\theta}^{B}_{IB}\times\underline{x}^{B2}_{p_2/b} \qquad \Delta\underline{x}^{B1}_{b/a} = \Delta\underline{\chi}^{B}_{b/a} + \Delta\underline{\theta}^{B}_{IB}\times\underline{x}^{B2}_{b_2/a} \tag{9}$$

We then let the $\Delta$ changes become the infinitesimally small "*d*" differentials: $\underline{x}^{B2}_{p2/b} \to \underline{x}^{B}_{p/b}$, $\underline{x}^{B2}_{b2/a} \to \underline{x}^{B}_{b/a}$, $\Delta\underline{x}^{B1}_{b/a} \to d\underline{x}^{B}_{b/a}$, $\Delta\underline{\chi}^{B}_{b/a} \to d\underline{\chi}^{B}_{b/a}$, $\Delta\underline{\theta}^{B}_{IB} \to d\underline{\theta}^{B}_{IB}$. Thus, (9) becomes

$$d\underline{x}^{B}_{p/b} = d\underline{\chi}^{B}_{p/b} + d\underline{\theta}^{B}_{IB} \times \underline{x}^{B}_{p/b} \qquad d\underline{x}^{B}_{b/a} = d\underline{\chi}^{B}_{b/a} + d\underline{\theta}^{B}_{IB} \times \underline{x}^{B}_{b/a} \tag{10}$$

Finally, since all vectors in (1) are defined in *B* frame coordinates, we can dispense with the superscript notation to obtain the simplified form

$$d\underline{x}_{p/b} = d\underline{\chi}_{p/b} + d\underline{\theta}_{IB} \times \underline{x}_{p/b} \qquad d\underline{x}_{b/a} = d\underline{\chi}_{b/a} + d\underline{\theta}_{IB} \times \underline{x}_{b/a} \tag{11}$$

where $d\underline{\chi}_{p/b}$ is the differential position change of point *p* observed at point *b* in rotating coordinates, $d\underline{x}_{p/b}$ is the differential position change of point *p* observed at point *b* in a non-rotating coordinate frame that is instantaneously aligned with the rotating frame, $d\underline{\chi}_{b/a}$ is the differential position change of point *b* observed at point *a* in rotating coordinates, and $d\underline{x}_{b/a}$ is the differential position change of point *b* observed at point *a* in a non-rotating coordinate frame that is instantaneously aligned with the rotating frame.

Similarly, we can also look at the differential form of (3):

$$d\underline{x}_{p/a} = d\underline{x}_{p/b} + d\underline{x}_{b/a} \tag{12}$$

Substituting $d\underline{x}_{p/b}$ and $d\underline{x}_{b/a}$ from (11) into (12) then obtains the general result:

$$d\underline{x}_{p/a} = d\underline{\chi}_{p/b} + d\underline{\theta}_{IB} \times \underline{x}_{p/b} + d\underline{\chi}_{b/a} + d\underline{\theta}_{IB} \times \underline{x}_{b/a} \tag{13}$$

Relativity theory deals with variations from traditional Galilean kinematics when observations of distant events are determined by observers travelling relative to one another [2 Chpt V1 Sect 2; 3; 8]. In the current development, (12) fits into this category because it involves kinematic measurements made at point *a* (i.e., distant events $d\underline{x}_{p/a}$ and $d\underline{x}_{b/a}$) and their relationship with a measurement made at point *b* (i.e., $d\underline{x}_{p/b}$), point *b* being in motion relative to point *a*. But, Appendix A shows that (12) is identical to what would be obtained from Relativity theory when the differential distance travelled by observation point *b* relative to observation point *a* (i.e., $\left|d\underline{x}_{b/a}\right|$) is small compared to the distance a photon would travel (at the speed of light) over the time interval for $d\underline{x}_{b/a}$ differential motion. On the other hand, Relativity theory does not apply for each of the $d\underline{x}_{p/b}$ and $d\underline{x}_{b/a}$ expressions in (11) substituted in (12) because each is derived from measurements made separately at either the *a* or *b* observation points.

Thus, under normal operating conditions, (13) derived from (11) and (12, is generally compatible with both Galilean/Newtonian and Relativity kinematic theory.

## APPLICATION TO A RIGID BODY AND A PARTICULAR OBSERVATION POINT SELECTION

Anticipating its application to optical gyros, we first specialize observation point *b* to be located at the starting point of $d\underline{x}_{p/b}$ differential motion. Then $\underline{x}_{p/b} \approx 0$, and (13) simplifies to

$$d\underline{x}_{p/a} = d\underline{\chi}_{p/b} + d\underline{\chi}_{b/a} + d\underline{\theta}_{IB} \times \underline{x}_{b/a} \tag{14}$$

For a rigid rotating body, there is no movement between points fixed within the body. Thus, if we now define points *a* and *b* to be fixed to the rotating body, $d\underline{\chi}_{b/a} = 0$. Eq. (14) thereby reduces to

$$d\underline{x}_{p/a} = d\underline{\chi}_{p/b} + d\underline{\theta}_{IB} \times \underline{x}_{b/a} \tag{15}$$

Eq. (15 is a fundamental equation describing the differential position change $d\underline{x}_{p/a}$ of an arbitrary point *p* that would be measured in non-rotating coordinates at point *a* within the body, as a function of $d\underline{\chi}_{p/b}$, the *p* motion that would be measured in rotating coordinates at point *b* within the body, the differential angular rotation $d\underline{\theta}_{IB}$ of the body relative to inertial space during the *p* motion, and the distance vector $\underline{x}_{b/a}$ from point *a* to point *b*. Since (15) was derived from (13), it is also compatible with traditional vector kinematic theory, and under normal operating conditions, Relativity theory.

The equivalent to (15) in terms of $d\underline{x}_{p/a}$ and $d\underline{\chi}_{p/b}$ magnitudes is derived by taking the dot product of (15) with itself:

$$\begin{aligned} d\underline{x}_{p/a} \cdot d\underline{x}_{p/a} &= \left(d\underline{\chi}_{p/b} + d\underline{\theta}_{IB} \times \underline{x}_{b/a}\right) \cdot \left(d\underline{\chi}_{p/b} + d\underline{\theta}_{IB} \times \underline{x}_{b/a}\right) \\ = d\underline{\chi}_{p/b} \cdot d\underline{\chi}_{p/b} &+ 2d\underline{\chi}_{p/b} \cdot \left(d\underline{\theta}_{IB} \times \underline{x}_{b/a}\right) + \left(d\underline{\theta}_{IB} \times \underline{x}_{b/a}\right) \cdot \left(d\underline{\theta}_{IB} \times \underline{x}_{b/a}\right) \\ &\approx d\underline{\chi}_{p/b} \cdot d\underline{\chi}_{p/b} + 2d\underline{\chi}_{p/b} \cdot \left(d\underline{\theta}_{IB} \times \underline{x}_{b/a}\right) \end{aligned} \tag{16}$$

Dividing (16) by $d\underline{\chi}_{p/b} \cdot d\underline{\chi}_{p/b}$ finds

$$\frac{d\underline{x}_{p/a}\cdot d\underline{x}_{p/a}}{d\underline{\chi}_{p/b}\cdot d\underline{\chi}_{p/b}}=1+2\frac{d\underline{\chi}_{p/b}\cdot\left(d\underline{\theta}_{IB}\times\underline{x}_{b/a}\right)}{d\underline{\chi}_{p/b}\cdot d\underline{\chi}_{p/b}} \tag{17}$$

Recognizing that the magnitudes of $d\underline{x}_{p/a}$ and $d\underline{\chi}_{p/b}$ are the square roots of $d\underline{x}_{p/a}\cdot d\underline{x}_{p/a}$ and $d\underline{\chi}_{p/b}\cdot d\underline{\chi}_{p/b}$ then obtains for the square root of (17):

$$\frac{\left|d\underline{x}_{p/a}\right|}{\left|d\underline{\chi}_{p/b}\right|}=\sqrt{\frac{d\underline{x}_{p/a}\cdot d\underline{x}_{p/a}}{d\underline{\chi}_{p/b}\cdot d\underline{\chi}_{p/b}}}\approx 1+\frac{d\underline{\chi}_{p/b}\cdot\left(d\underline{\theta}_{IB}\times\underline{x}_{b/a}\right)}{\left|d\underline{\chi}_{p/b}\right|\left|d\underline{\chi}_{p/b}\right|}=1+\frac{\left(\underline{x}_{b/a}\times d\underline{\chi}_{p/b}\right)\cdot d\underline{\theta}_{IB}}{\left|d\underline{\chi}_{p/b}\right|\left|d\underline{\chi}_{p/b}\right|} \tag{18}$$

APPLICATION TO AN OPTICAL GYRO

For the analysis of a rotating optical gyro, point *p* will represent a photon of light travelling in a waveguide fixed within the gyro (the rigid body). We also define another photon *q* travelling within the same waveguide, but in the opposite direction from photon *p*. The analysis begins from (18) with the derivation of optical gyro equations related to photon *p* motion. The same approach will then be used to derive the corresponding equations for photon *q*.

As shown in Fig. 2, the magnitude of $\underline{x}_{b/a}\times d\underline{\chi}_{p/b}$ in (18) is twice the area $dA_p$ of the triangle formed by $\underline{x}_{b/a}$ and $d\underline{\chi}_{p/b}$ between points *a*, *b*, and *p*.

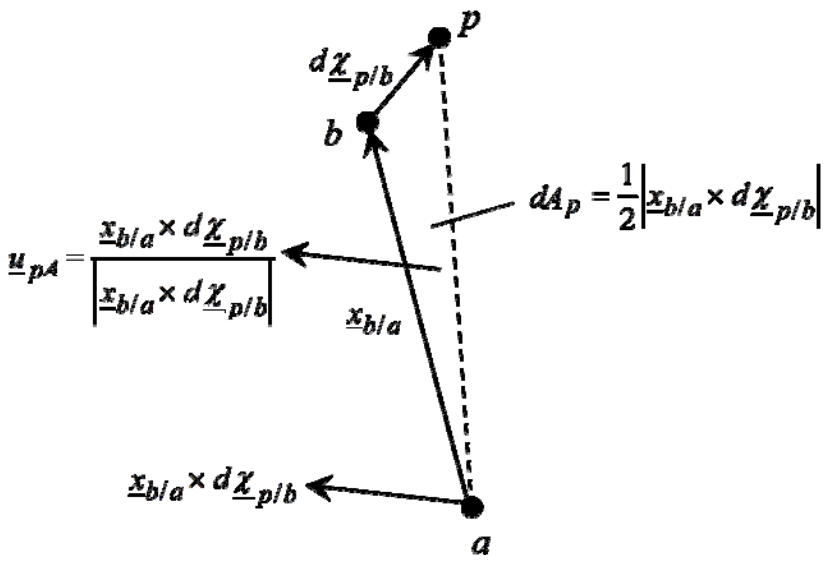


Fig. 2 - Triangular Area Formed By $\underline{x}_{b/a}$ And $d\underline{\chi}_{p/b}$

Identifying $\underline{u}_{pA}$ as the unit vector in Fig. 2 parallel to the $\frac{1}{2}\underline{x}_{b/a}\times d\underline{\chi}_{p/b}$ area vector, and $\underline{u}_{Inpt_p}$, the negative of $\underline{u}_{pA}$, as the gyro input axis for angular rotation generated by *p* photon motion, then finds for $\left(\underline{x}_{p/a}\times d\underline{\chi}_{p/b}\right).d\underline{\theta}_p$ in (18):

$$\left(\underline{x}_{p/a}\times d\underline{\chi}_{p/b}\right).d\underline{\theta}_p = 2\,dA_p\,\underline{u}_{pA}.d\underline{\theta}_p = -2\,dA_p\,\underline{u}_{Inpt_p}.d\underline{\theta}_p = -2\,dA_p\,d\theta_{p_{Inpt}} \quad (19)$$

where $d\underline{\theta}_p$ is the particular $d\underline{\theta}_{IB}$ value during *p* photon differential motion ($d\underline{\theta}_q$ will be used subsequently to identify the $d\underline{\theta}_{IB}$ value during *q* photon motion), and $d\theta_{Inpt_p}$ is the component of $d\underline{\theta}_p$ along $\underline{u}_{Inpt_p}$, the incremental rotation component being measured by the gyro. Substituting (19) in (18) then obtains

$$\frac{\left|d\underline{x}_{p/a}\right|}{\left|d\underline{\chi}_{p/b}\right|} = 1-2\frac{dA_p\,d\theta_{p_{Inpt}}}{\left|d\underline{\chi}_{p/b}\right|\left|d\underline{\chi}_{p/b}\right|} = 1-2\frac{dA_p}{dL_p}\frac{d\theta_{p_{Inpt}}}{dL_p} \quad (20)$$

where $dL_p$ is the differential distance moved by photon *p* relative to the rotating gyro waveguide during the $d\theta_{p_{Inpt}}$ rotation.

Now consider the other photon *q* traveling along the same waveguide as photon *p*, but in the opposite direction. Identifying observation point $b'$ (analogous to point *b* in Fig. 2 for *p* photon motion) as the point in the waveguide where photon *q* is instantaneously located, the equivalent to (20) derives similar to (15) – (20) as

$$d\underline{x}_{q/a} = d\underline{\chi}_{q/b'} + d\underline{\theta}_{IB}\times\underline{x}_{b'/a} \quad (21)$$

$$d\underline{x}_{q/a}.d\underline{x}_{q/a} \approx d\underline{\chi}_{q/b'}.d\underline{\chi}_{q/b'} + 2d\underline{\chi}_{q/b'}.\left(d\underline{\theta}_{IB}\times\underline{x}_{b'/a}\right) \quad (22)$$

$$\frac{d\underline{x}_{q/a}.d\underline{x}_{q/a}}{\underline{\chi}_{q/b'}.d\underline{\chi}_{q/b'}} = 1+2\frac{d\underline{\chi}_{q/b'}.\left(d\underline{\theta}_{IB}\times\underline{x}_{b'/a}\right)}{d\underline{\chi}_{q/b'}.d\underline{\chi}_{q/b'}} \quad (23)$$

$$\frac{\left|d\underline{x}_{q/a}\right|}{\left|d\underline{\chi}_{q/b'}\right|} = 1+\frac{\left(\underline{x}_{b'/a}\times d\underline{\chi}_{q/b'}\right).d\underline{\theta}_{IB}}{\left|d\underline{\chi}_{q/b'}\right|\left|d\underline{\chi}_{q/b'}\right|} \quad (24)$$

$$\left(\underline{x}_{b'/a} \times d\underline{\chi}_{q/b'}\right) . d\underline{\theta}_q = 2\, dA_q\, \underline{u}_{qA} . d\underline{\theta}_q = 2\, dA_q\, \underline{u}_{Inpt_q} . d\underline{\theta}_q = 2\, dA_q\, d\theta_{q_{Inpt}} \quad (25)$$

leading to

$$\frac{\left|d\underline{x}_{q/a}\right|}{\left|d\underline{\chi}_{q/b'}\right|} = 1 + 2\frac{dA_q}{dL_q}\frac{d\theta_{q_{Inpt}}}{dL_q} \quad (26)$$

where $d\underline{\chi}_{q/b'}$ is the differential change in the position of photon *q* relative to observation point $b'$ instantaneously fixed within the rotating waveguide, $d\underline{x}_{q/a}$ is the differential change in the position of photon *q* that would be observed at point *a* in a non-rotating coordinate frame that is instantaneously aligned with the rotating gyro frame, $d\underline{\theta}_q$ is the particular $d\underline{\theta}_{IB}$ incremental vector of gyro angular rotation during point *q* distance traversal $d\underline{x}_{q/a}$ and $d\underline{\chi}_{q/b'}$, $\underline{u}_{qA}$ is a unit vector perpendicular to the triangular area $dA_q$ traced out by photon *q* as it travels from point $b'$around point *a* (see Fig. 3), $\underline{u}_{Inpt_q}$ is a unit vector along the *q* photon input axis (and parallel to $\underline{u}_{qA}$), $d\theta_{q_{Inpt}}$ is the *q* photon motion input axis component of $d\underline{\theta}_q$ along $\underline{u}_{Inpt_q}$, and $dL_q$ is the differential distance traversed by photon *q* relative to the rotating gyro waveguide during $d\theta_{q_{Inpt}}$ rotation (and the magnitude of $d\underline{\chi}_{q/b'}$). Note the polarity difference between

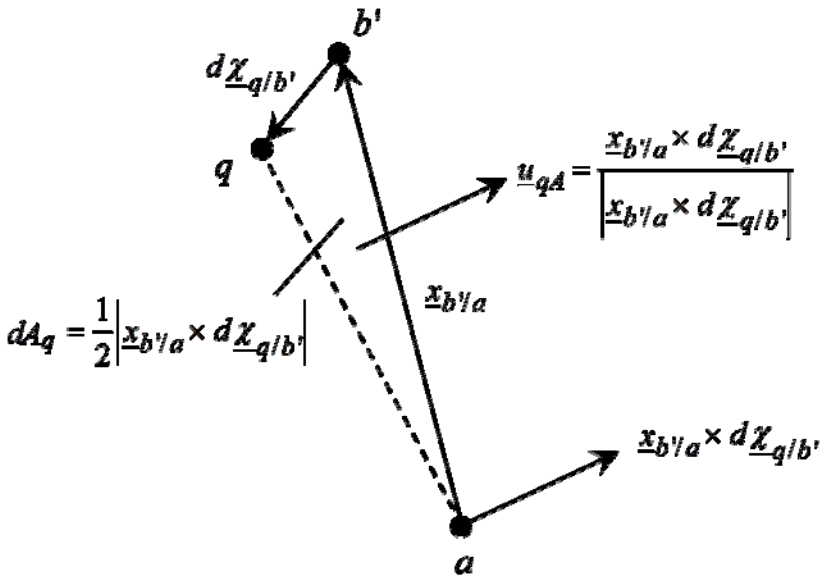


Fig. 3 - Triangular Area Formed By $\underline{x}_{b'/a}$ And $d\underline{\chi}_{q/b'}$

$\underline{u}_{Inpt_q}$ in (25) for *q* photon motion compared with $\underline{u}_{Inpt_p}$ in (19) for photon *p* motion. The difference corresponds to the opposite *p* and *q* travel directions, thereby traversing area vectors in opposite direction (compare Fig. 3 for photon *q* with Fig. 2 for photon *p*).

WAVELENGTH EQUIVALENCE

An equivalence between wavelengths for *p* and *q* photon motion can be determined by first expanding the $\left|d\underline{x}_{p/a}\right|$, $\left|d\underline{\chi}_{p/b}\right|$, $\left|d\underline{x}_{q/a}\right|$ , $\left|d\underline{\chi}_{q/b'}\right|$ distance differentials in (20) and (26) to represent small finite $\Delta$ distances measured at points *a* and *b* during passage of a light wave observed at points *a* and *b*, i.e., $\left|d\underline{x}_{p/a}\right| \to \left|\Delta\underline{x}_{p/a}\right|$, $\left|d\underline{\chi}_{p/b}\right| \to \left|\Delta\underline{\chi}_{p/b}\right|$, $\left|d\underline{x}_{q/a}\right| \to \left|\Delta\underline{x}_{q/a}\right|$, $\left|d\underline{\chi}_{q/b'}\right| \to \left|\Delta\underline{\chi}_{q/b'}\right|$. Thus, from (20) and (26):

$$\frac{\left|\Delta\underline{x}_{p/a}\right|}{\left|\Delta\underline{\chi}_{p/b}\right|} = 1 - 2\frac{dA_p}{dL_p}\frac{d\theta_{p_{Inpt}}}{dL_p} \qquad \frac{\left|\Delta\underline{x}_{q/a}\right|}{\left|\Delta\underline{\chi}_{q/b'}\right|} = 1 + 2\frac{dA_q}{dL_q}\frac{d\theta_{q_{Inpt}}}{dL_q} \qquad (27)$$

We now identify the $\Delta$ distances in (27) as representing the movement of the *p* and *q* photons through a distance of one wavelength as measured at points *a* and *b*. (Note: The start and end of a wave, e.g., are events that are observable at points *a* and *b*. For example, if *b* is defined to be at the leading edge of a *p* wave, $\left|\Delta\underline{\chi}_{p/b}\right|$ can be directly measured as the change in the leading edge position when the wave's trailing edge reaches *b*.) Recognizing that the wavelength of a *p* or *q* photon light wave will be the same when measured in non-rotating inertial space at point *a* (e.g., as, $\left|\Delta\underline{x}_{p/a}\right|$ and $\left|\Delta\underline{x}_{q/a}\right|$) we can then write

$$\left|\Delta\underline{x}_{p/a}\right| = \lambda_0 \qquad \left|\Delta\underline{\chi}_{p/b}\right| = \lambda_{p/b} \qquad \left|\Delta\underline{x}_{q/a}\right| = \lambda_0 \qquad \left|\Delta\underline{\chi}_{q/b'}\right| = \lambda_{q/b'} \qquad (28)$$

where $\lambda_{p/b}$, $\lambda_{q/b'}$ are wavelengths of the *p* and *q* light waves measured at points *b* and $b'$ in the waveguide fixed to the rotating gyro, and $\lambda_0$ is the wavelength of the *p* and *q* light waves measured at point *a* in non-rotating inertial space. Substituting (28) in (27) then finds with rearrangement

$$\lambda_{p/b} = \lambda_0 \Big/ \left(1 - 2\frac{dA_p}{dL_p}\frac{d\theta_{p_{Inpt}}}{dL_p}\right) \qquad \lambda_{q/b'} = \lambda_0 \Big/ \left(1 + 2\frac{dA_q}{dL_q}\frac{d\theta_{q_{Inpt}}}{dL_q}\right) \qquad (29)$$

Eqs. (19) shows that for positive angular input relative to the rotating waveguide (i.e., positive $d\theta_{p_{Inpt}}$ and $d\theta_{q_{Inpt}}$), the wavelength $\lambda_{p/b}$ of the $p$ wave at point $b$ will increase and the wavelength $\lambda_{q/b'}$ of the $q$ wave at point $b'$ will decrease compared with $\lambda_0$, the wavelength of the same light waves that would be measured in non-rotating inertial space at point $a$.

## LIGHT WAVE EQUIVALENCE IN NON-ROTATING COORDINATES

The $p$ and $q$ photons can also be considered as vectors within monochromatic light waves that propagate at the speed of light along the waveguide. The photon vector is defined to be perpendicular to the light wave travel path with its direction defining the light wave polarization state at that point along the wave. To translate $p$ and $q$ counter-travelling photon kinematics into travelling wave equivalents, first consider wave equations under zero angular rotation at a common point in the waveguide as in [9 pp 428]:

$$g_{p_{wav}} = B\sin\left\{\left[2\pi\left(c\,t_p - s\right)/\lambda_0\right] + \beta_p\right\}$$
$$= B\sin\left(\frac{2\pi c\,t_p}{\lambda_0} - \frac{2\pi s}{\lambda_0} + \beta_p\right) = B\sin\left(\int_0^{t_p} 2\pi f_0\,dt - \frac{2\pi s}{\lambda_0} + \beta_p\right)$$
$$g_{q_{wav}} = B\sin\left\{\left[2\pi\left(c\,t_q + s\right)/\lambda_0\right] + \beta_q\right\} \qquad (30)$$
$$= B\sin\left(\frac{2\pi c\,t_q}{\lambda_0} + \frac{2\pi s}{\lambda_0} + \beta_q\right) = B\sin\left(\int_0^{t_q} 2\pi f_0\,dt + \frac{2\pi s}{\lambda_0} + \beta_q\right)$$

In (30), $g_{p_{wav}}$ and $g_{q_{wav}}$ are monochromatic light wave functions within the gyro contained waveguide ($g_{p_{wav}}$ for the wave travelling in the direction of $p$ photon motion, $g_{q_{wav}}$ for the wave travelling in the direction of $q$ photon motion), $B$ is the light wave amplitude (assumed the same for the $p$ and $q$ light waves), $\lambda_0$ is the wavelength of the light waves under zero gyro rotation rate at point $a$ (and elsewhere under zero angular rate), $s$ is the distance in the waveguide from a defined reference point to another point where the $g_{p_{Wav}}$ and $g_{q_{Wav}}$ wave functions in (30) are to be measured (the "readout zone"), $t_p$ and $t_q$ are time intervals for $p$ and $q$ travel along the waveguide from the starting reference position on the waveguide (now analytically defined being where $s = 0$), $dt$ is the differential time change for differential distance movements of the $p$ and $q$ photon waves during their travel around the waveguide, $\beta_p, \beta_q$ are $p$ and $q$ light wave phase angles at times $t_p$, $t_q$ and location $s$, and $f_0$ is the frequency of a light wave having $\lambda_0$ wavelength and propagating in non-rotating space at the speed of light $c$ (i.e., $f_0 = c/\lambda_0$). The $\beta_p, \beta_q$ phase angles include initial values (at $t_p$, $t_q$ = 0) plus phase changes accumulated along the wave path from path length variations from nominal (intentional or

unintentional). The $c t_p$ and $c t_q$ terms in (30) indicate a $g_{p_{wav}}$ wave travelling in the direction of positive *s*, and a $g_{q_{wav}}$ travelling in the direction of negative *s*.

## LIGHT WAVE EQUIVALENCE IN ROTATING COORDINATES

The analytical development thus far has been based on classical vector kinematics to describe $d\underline{\chi}_{p/b}$ motion. To extend (30) into its form under rotation (and a wave solution matching actual optical gyro test data) requires introducing the theory of Relativity into the derivation process. The intent is to equate counter travelling light wave locations relative to the rotating waveguide at a common point in time (i.e., in Relativity parlance, the wave intersection at the same space-time location). To this end, let us first define $d\underline{x}_{p/b}$ as the differential change in the position of point *p* that would be observed at point *b* in a non-rotating coordinate frame that is instantaneously aligned with the rotating gyro frame, and $dt_{p_b}$ as the differential time interval that would register on a clock located at point *b* fixed within the rotating waveguide. A basic premise of Relativity theory [1 Part 1 Chpt 11] is that the speed of a photon measured at any point in non-rotating space will equal the same speed of light constant *c*, thus, $\left|d\underline{x}_{p/b}\right| = c\ dt_{p_b}$ - See [6 Appndx A] for an analytical demonstration and [3] for its analytical basis. Similarly, for photon *q* and its motion in non-rotating space relative to point $b'$, $\left|d\underline{x}_{q/b'}\right| = c\ dt_{q_{b'}}$ where $dt_{q_{b'}}$ is the differential time interval that would register on a clock located at point $b'$ within the rotating gyro fixed waveguide.

Now consider from (11) that $d\underline{\chi}_{p/b} = d\underline{x}_{p/b} - d\underline{\theta}_p \times \underline{x}_{p/b}$, where $\underline{x}_{p/b}$ is the distance vector from point *b* to *p*. Since *b* was defined to be at the $d\underline{x}_{p/b}$ starting point, $\underline{x}_{p/b} = d\underline{x}_{p/b}$, hence, $d\underline{\chi}_{p/b} = d\underline{x}_{p/b} - d\underline{\theta}_p \times d\underline{x}_{p/b} \approx d\underline{x}_{p/b}$. Similarly, $d\underline{\chi}_{q/b'} = d\underline{x}_{q/b'}$ for photon *q*. Thus, since $\left|d\underline{x}_{p/b}\right| = c\ dt_{p_b}$ and $\left|d\underline{x}_{q/b'}\right| = c\ dt_{q_{b'}}$ as discussed in the previous paragraph, it follows that

$$\left|d\underline{\chi}_{p/b}\right| = c\ dt_{p_b} \qquad \left|d\underline{\chi}_{q/b'}\right| = c\ dt_{q_{b'}} \tag{31}$$

We will be evaluating both the *p* and the *q* wave solutions in rotating coordinates under the "same" conditions which we now define as the "same" differential movements of photons *p* and *q*, i.e., for $\left|d\underline{\chi}_{p/b}\right| = \left|d\underline{\chi}_{q/b'}\right|$. From (31), this also corresponds to the same time interval $dt_{p_b}$ for *p* photon motion as $dt_{q_{b'}}$ for *q* motion. Anticipating the extension of (30) to rotating gyro space (and to limit the number of newly defined parameters), we choose to represent the equal

$dt_{p_b}$ and $dt_{q_{b'}}$ values in (31) by parameter $dt$ in (30). It then also follows that $dL_p \equiv \left| d\underline{\chi}_{p/b} \right|$ and $\left| d\underline{\chi}_{q/b'} \right| \equiv dL_q$ in (31) will equate to $c\,dt$. Finally, now that it has been established that the *p* and *q* photons will be travelling at the speed of light constant *c* relative to the rotating gyro waveguide, we can show that frequencies $f_{p/b}$ and $f_{q/b'}$ associated with the (29) wavelengths $\lambda_{p/b}$, $\lambda_{q/b'}$ will be

$$f_{p/b} = \frac{c}{\lambda_{p/b}} = \frac{c}{\lambda_0}\left(1 - 2\frac{dA_p}{dL_p}\frac{d\theta_{p_{Inpt}}}{c\,dt}\right) \qquad f_{q/b'} = \frac{c}{\lambda_{q/b'}} = \frac{c}{\lambda_0}\left(1 + 2\frac{dA_q}{dL_q}\frac{d\theta_{q_{Inpt}}}{c\,dt}\right) \quad (32)$$

Eqs. (32) show that relative to the waveguide in the rotating gyro, the frequency $f_{p/b}$ of the *p* photon light wave at point *b* will decrease under positive sensed angular rate $d\theta_{p_{Inpt}}/dt$ while the frequency $f_{q/b'}$ of the *q* photon light wave at point $b'$ will increase under positive sensed angular rate $d\theta_{q_{Inpt}}/dt$.

Returning to (30), recall that $f_0$ for $g_{p_{wav}}$ and $g_{q_{wav}}$ represents the frequency of the *p*, *q* light waves under zero angular rate. Rotation will cause $f_0$ in (30) to change to $f_{p/b}$ for photon *p* at location *b* in the waveguide, and to $f_{q/b'}$ for photon *q* at location $b'$. Similarly, $\lambda_0$ for *p* and *q* in (30) will change to the $\lambda_{p/b}$ and $\lambda_{q/b'}$ values in (29), but assuming small *s* in (30), can be approximated under rotation by $\lambda_0$. We also assume that the (30) wave functions will be evaluated for equal $t_p$ and $t_q$ values, call it $t_{wav}$. Thus, the equivalent to (30) under rotation will become

$$\begin{aligned} g_{p_{wav}} &= B\sin\left(\textstyle\int_0^{t_{wav}} 2\pi f_{p/b}\,dt - \dfrac{2\pi s}{\lambda_0} + \beta_p\right) \\ g_{q_{wav}} &= B\sin\left(\textstyle\int_0^{t_{wav}} 2\pi f_{q/b'}\,dt + \dfrac{2\pi s}{\lambda_0} + \beta_q\right) \end{aligned} \quad (33)$$

Now we can substitute $f_{p/b}$ and $f_{q/b'}$ from (32) into (33) to find

$$\begin{aligned} g_{p_{wav}} &= B\sin\left[\frac{2\pi}{\lambda_0}\left(c\,t_{wav} - 2\textstyle\int_0^{t_{wav}} \dfrac{dA_p}{dL_p}\,d\theta_{p_{Inpt}}\right) - \dfrac{2\pi s}{\lambda_0} + \beta_p\right] \\ &= B\sin\left[\frac{2\pi\left(c\,t_{wav} - s\right)}{\lambda_0} + \beta_p - \frac{4\pi}{\lambda_0}\textstyle\int_0^{t_{wav}} \dfrac{dA_p}{dL_p}\,d\theta_{p_{Inpt}}\right] \end{aligned} \quad (34)$$

(Continued)

$$g_{q_{wav}} = B\sin\left[\frac{2\pi}{\lambda_0}\left(c\,t_{wav} + 2\int_0^{t_{wav}} \frac{dA_q}{dL_q}\,d\theta_{q_{Inpt}}\right) + \frac{2\pi s}{\lambda_0} + \beta_q\right]$$
$$= B\sin\left[\frac{2\pi\left(c\,t_{wav}+s\right)}{\lambda_0} + \beta_q + \frac{4\pi}{\lambda_0}\int_0^{t_{wav}} \frac{dA_q}{dL_q}\,d\theta_{q_{Inpt}}\right] \quad (34)\ (\text{Concluded})$$

The integral terms in (34) show the effect of rotation in optical gyros as a building in the phase difference between the *p* and *q* travelling waves from their common $2\pi c\,t_{wav}/\lambda_0$ accumulating phase under zero angular rate. Under positive angular rate, the *p* wave phase will be reduced by $\frac{4\pi}{\lambda_0}\int_0^{t_{wav}} \frac{dA_p}{dL_p}\,d\theta_{p_{Inpt}}$ and the *q* wave phase will be increased by $\frac{4\pi}{\lambda_0}\int_0^{t_{wav}} \frac{dA_q}{dL_q}\,d\theta_{q_{Inpt}}$.

COMBINED OPPOSITELY DIRECTED WAVES IN THE READOUT ZONE

Because the *p* and *q* waves occupy the same space in the waveguide their wave functions will add in the readout zone to form

$$h_{wav} \equiv g_{p_{wav}} + g_{q_{wav}}$$
$$= B\sin\left[\frac{2\pi\left(c\,t_{wav}-s\right)}{\lambda_0} + \beta_p - \frac{4\pi}{\lambda_0}\int_0^{t_{wav}} \frac{dA_p}{dL_p}\,d\theta_{p_{Inpt}}\right]$$
$$+B\sin\left[\frac{2\pi\left(c\,t_{wav}+s\right)}{\lambda_0} + \beta_q + \frac{4\pi}{\lambda_0}\int_0^{t_{wav}} \frac{dA_q}{dL_q}\,d\theta_{q_{Inpt}}\right]$$
$$= 2B\sin\frac{1}{2}\left[\begin{array}{l}\dfrac{2\pi\left(c\,t_{wav}-s\right)}{\lambda_0} + \beta_p - \dfrac{4\pi}{\lambda_0}\int_0^{t_{wav}} \dfrac{dA_p}{dL_p}\,d\theta_{p_{Inpt}} \\ +\dfrac{2\pi\left(c\,t_{wav}+s\right)}{\lambda_0} + \beta_q + \dfrac{4\pi}{\lambda_0}\int_0^{t_{wav}} \dfrac{dA_q}{dL_q}\,d\theta_{q_{Inpt}}\end{array}\right]\times$$
$$\cos\frac{1}{2}\left[\begin{array}{l}\dfrac{2\pi\left(c\,t_{wav}-s\right)}{\lambda_0} + \beta_p - \dfrac{4\pi}{\lambda_0}\int_0^{t_{wav}} \dfrac{dA_p}{dL_p}\,d\theta_{p_{Inpt}} \\ -\dfrac{2\pi\left(c\,t_{wav}+s\right)}{\lambda_0} - \beta_q - \dfrac{4\pi}{\lambda_0}\int_0^{t_{wav}} \dfrac{dA_q}{dL_q}\,d\theta_{q_{Inpt}}\end{array}\right] \quad (35)$$

(Continued)

$$= 2B \sin\left[\frac{2\pi c\, t_{wav}}{\lambda_0} + \frac{\beta_p + \beta_q}{2} - \frac{2\pi}{\lambda_0}\int_0^{t_{wav}}\left(\frac{dA_p}{dL_p}\, d\theta_{p_{Inpt}} - \frac{dA_q}{dL_q}\, d\theta_{q_{Inpt}}\right)\right]\times$$
$$\cos\left[-\frac{2\pi s}{\lambda_0} + \frac{\beta_p - \beta_q}{2} - \frac{2\pi}{\lambda_0}\int_0^{t_{wav}}\left(\frac{dA_p}{dL_p}\, d\theta_{p_{Inpt}} + \frac{dA_q}{dL_q}\, d\theta_{q_{Inpt}}\right)\right]$$
$$= 2B \sin\left[\frac{2\pi c\, t_{wav}}{\lambda_0} + \frac{\beta_p + \beta_q}{2} - \frac{2\pi}{\lambda_0}\int_0^{t_{wav}}\left(\frac{dA_p}{dL_p}\, d\theta_{p_{Inpt}} - \frac{dA_q}{dL_q}\, d\theta_{q_{Inpt}}\right)\right]\times$$
$$\cos\left[\frac{2\pi s}{\lambda_0} - \frac{\beta_p - \beta_q}{2} + \frac{2\pi}{\lambda_0}\int_0^{t_{wav}}\left(\frac{dA_p}{dL_p}\, d\theta_{p_{Inpt}} + \frac{dA_q}{dL_q}\, d\theta_{q_{Inpt}}\right)\right] \quad \text{(35) (Concluded)}$$

where $h_{wav}$ is a combined $p$ and $q$ wave function. (Note that (35) assumes that the $g_{p_{wav}}$ and $g_{q_{wav}}$ functions lie in the same plane around the waveguide at the same instant of time so that they add algebraically as shown. A part of optical gyro design is based on meeting this requirement.)

The normalized power $W$ in the combined (35) optical beam signal is proportional to the square of $h_{Wav}$ in (35):

$$W \equiv \frac{h_{wav}^2}{B^2} = 4\sin^2\left[\frac{2\pi c\, t_{wav}}{\lambda_0} + \frac{\beta_p + \beta_q}{2} - \frac{2\pi}{\lambda_0}\int_0^{t_{wav}}\left(\frac{dA_p}{dL_p}\, d\theta_{p_{Inpt}} - \frac{dA_q}{dL_q}\, d\theta_{q_{Inpt}}\right)\right]\times$$
$$\cos^2\left[\frac{2\pi s}{\lambda_0} - \frac{\beta_p - \beta_q}{2} + \frac{2\pi}{\lambda_0}\int_0^{t_{wav}}\left(\frac{dA_p}{dL_p}\, d\theta_{p_{Inpt}} + \frac{dA_q}{dL_q}\, d\theta_{q_{Inpt}}\right)\right] \quad (36)$$

or with trigonometric expansion,

$$W = \left\{1 - \cos\left[\frac{4\pi c}{\lambda_0} t_{wav} + \beta_p + \beta_q - \frac{4\pi}{\lambda_0}\int_0^{t_{wav}}\left(\frac{dA_p}{dL_p}\, d\theta_{p_{Inpt}} - \frac{dA_q}{dL_q}\, d\theta_{q_{Inpt}}\right)\right]\right\}\times$$
$$\left\{1 + \cos\left[\frac{4\pi s}{\lambda_0} - \left(\beta_p - \beta_q\right) + \frac{4\pi}{\lambda_0}\int_0^{t_{wav}}\left(\frac{dA_p}{dL_p}\, d\theta_{p_{Inpt}} + \frac{dA_q}{dL_q}\, d\theta_{q_{Inpt}}\right)\right]\right\} \quad (37)$$

Eq. (37) is the basis for the design of both ring laser and fiber optic gyros described next. It demonstrates that optical gyros are integrating instruments whose combined optical beam power $W$ measures the integral of differential changes in gyro angular orientation relative to non-rotating inertial space. The combined beam power illuminates photo detectors located in the waveguide readout zone, generating outputs of angular rotation increments by the gyro readout electronics.

RING LASER GYROS

A ring laser gyro (RLG) creates two oppositely directed beams of monochromatic light that traverse a closed optical path formed by three or more reflecting mirrors [10; 11]. The beams occupy the same physical space ("optical cavity") and are constrained to remain in a fixed "waveguide" relative to the gyro by an aperture and curved surface mirror(s). The concept is depicted in Fig. 4 for a 3-mirror RLG configuration, the individual laser beams identified as travelling in the clockwise (cw) and counter-clockwise (ccw) directions.

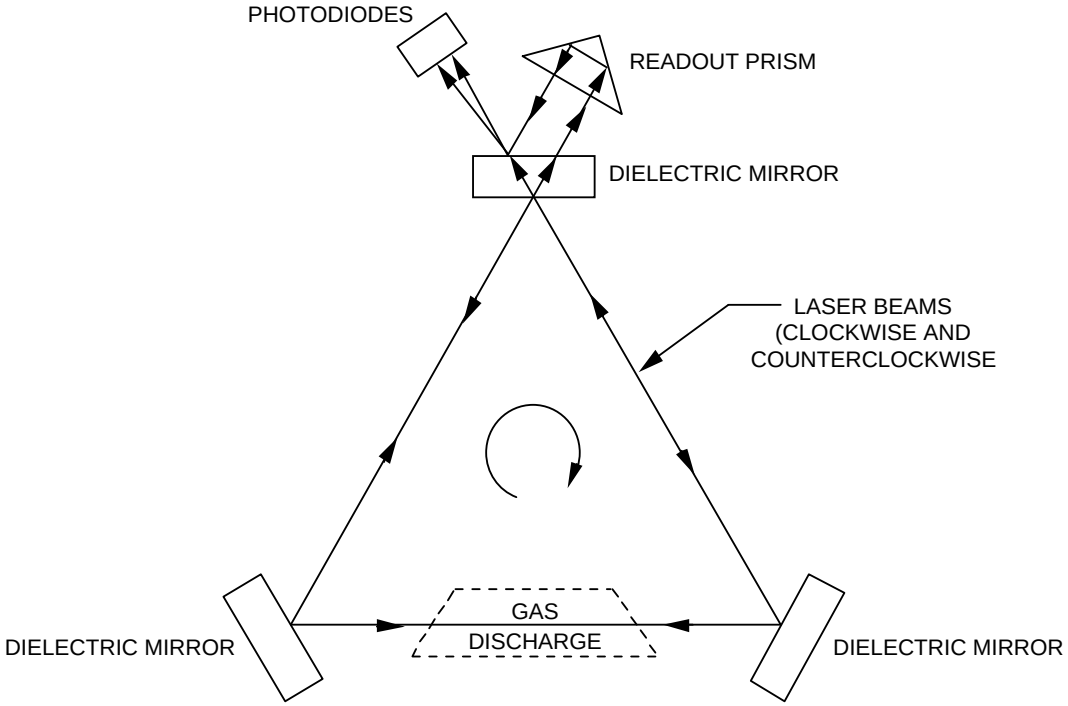


Fig. 4 - Ring Laser Gyro Operating Elements

The RLG light beams in Fig. 4 are sustained by the lasing action of a helium-neon gas discharge within the optical cavity. The reflecting surfaces are dielectric mirrors designed to selectively reflect the frequency associated with the particular helium-neon transition being used (typically of 0.63 micron wavelength). A small fraction of each beam escapes the cavity at the readout, one reflected through a corner prism, then recombined with the other on readout photo detectors. The corner prism is designed to produce a small angle between the recombining beams, thereby creating an optical interference fringe pattern on the photo detectors, each illuminated by a different portion of the fringe pattern. The fringe pattern is stationary under zero angular rotation of the cavity. Under cavity rotation, the fringes move across the photo detectors, generating a sinusoidal output at a frequency proportional to the gyro angular rate around its input axis (perpendicular to the plane of the Fig. 4 diagram). Photo detector readout logic converts the sinusoidal output into a digital square wave for each fringe passage. The rise and fall of the square wave edges generate output pulses, each representing an angular rotation through a known angular increment (the gyro output pulse scale factor). Two photo detectors are used, separated from each other by one quarter of a photo-detector-sensed fringe so that resulting

sinusoidal outputs are 90 deg phase separated. Comparison between photo detector generated square wave outputs determines the direction of rotation, positive or negative, depending on whether one square wave is leading or lagging the other.

Under zero rotation, the wavelength of the oppositely travelling light beams will be the same. Beam power loses in an RLG are compensated by lasing action within the helium/neon plasma, adding photons at the same wavelength in response to returning photons (i.e., through Light Amplification by the Stimulated Emission of Radiation – LASER [10; 11]). For the waves to form a closed continuous wave function, waves returning to the same point in the waveguide must be approximately in phase with the original waves. Otherwise, returning waves will tend to extinguish original waves, reducing beam amplitude and power. Minimizing the phase difference between returning and emitted light waves is achieved through a path length control (PLC) operation: A piezoelectric controlled micro-movement of one of the RLG mirrors (perpendicular its surface) to sustain maximum average light wave power, thus implicitly assuring that emitted photons will be in phase with returning photons. Average wave power is measured for the PLC control loop by a separate photo detector mounted on one of the mirror substrates.

As discussed previously, Relativity theory predicts that under rotation, the speed of each RLG light wave will be the same relative to a readout photo detector as it is in non-rotating space. As a consequence, (32) shows that the frequency of the RLG light beams will change, decreasing in Fig. 4 for the beam traveling with rotation, increasing for the oppositely travelling beam. Thus, rotation will cause returning waves to be phase shifted, tending to extinguish some of the original wave photons while leaving those intact having an integral number of wavelengths around the beam path. Adding photons by the helium/neon emission process compensates for this loss effect. But to sustain lasing, added photons must be of the same frequency as those in the return beams, i.e., at the rotation shifted frequency. Fortuitously, due to Doppler broadening [11], the RLG helium-neon transfer mechanism accommodates small frequency shifts induced by rotation, still providing photons to a returning wave at its shifted frequency over a narrow range around the frequency for zero-rotation.

RLG Analytical Model

In response to existing photons passing through the Fig. 4 helium-neon gas mixture, the RLG lasing process generates new $p$ and $q$ oppositely travelling photons at the same phase and frequency as the original. This creates the illusion that each photon is repeatedly traversing the wave path. The result is a combined beam amplitude power $W$ input to the photo detectors representing the integral of angular increments $d\theta_{p_{Inpt}}$ and $d\theta_{q_{Inpt}}$ in (37) from the time the photons were initially created. Thus, the integration time $t_{wav}$ in (37) represents the time since gyro turn-on when photons were originally created, and $\beta_p + \beta_q$ represents the combined initial phase between the Fig. 4 cw and ccw light beams at gyro turn-on.

With $t_{wav}$ representing the current time since gyro turn-on, Eq. (37) describes the normalized beam power of a standing wave in the readout zone created by addition of the $p$ and

*q* oppositely travelling light waves. The beam power amplitude is represented by the second bracketed { } term in (37) which is modulated by the first bracketed term { } at high frequency $c / \lambda_0$. At a given time $t_{wav}$, the second bracketed term varies cyclically with position *s*, generating nodes (zero amplitude points) across the readout zone (i.e., the "fringe pattern" discussed in the previous section) with a linear spacing between nodes of $\lambda_0 / 2$. The $\int_0^{t_{wav}} \left( \frac{dA_p}{dL_p} d\theta_{p_{Inpt}} + \frac{dA_q}{dL_q} d\theta_{q_{Inpt}} \right)$ integral term in (37) produces a translation of the standing wave pattern in the readout zone whose power amplitude repeats at a particular *s* location for each $\lambda_0 / 2$ change in the integral generated by angular rotation.

The two RLG photo detectors measure the *W* wave power in (37). For a typical RLG wavelength $\lambda_0$ of 0.63 microns, the frequency $2c / \lambda_0$ in the first (37) cosine term is high enough (2 × 3.0e8 / 0.63e-6 = 9.52 e14 Hz) to be eliminated by attenuation action of the readout electronics. Thus, (37) simplifies to

$$W = 1 + \cos\left[ \frac{4\pi s}{\lambda_0} - \left( \beta_p - \beta_q \right) + 2\pi \frac{2}{\lambda_0} \int_0^{t_{wav}} \left( \frac{dA_p}{dL_p} d\theta_{p_{Inpt}} + \frac{dA_q}{dL_q} d\theta_{q_{Inpt}} \right) \right] \quad (38)$$

The angular rotation sensing term $\int_0^{t_{wav}} \left( \frac{dA_p}{dL_p} d\theta_{p_{Inpt}} + \frac{dA_q}{dL_q} d\theta_{q_{Inpt}} \right)$ in (38) is the effect of Relativity generating a frequency difference between the counter-travelling light beams relative to their rotating waveguide container.

Eq. (38) describes the *W* power in the standing wave image formed in the Fig. 4 readout zone. The *s* parameter in (38) introduces phase shift in the cyclic *W* power distribution across the readout zone, producing the fringe pattern with nodes of zero power spaced at $\lambda_0 / 2$ intervals, interspersed with maximum power antinodes. Movement of the fringe pattern across the readout zone is represented by the integral term in (38) that continually adds phase shift to the *W* distribution in response to the integrated effect of gyro angular motion over time $t_{wav}$. The spatial position of each photo detector in Fig. 4 is represented in (38) by its particular *s* parameter location in the readout zone. By selecting the difference in photo detector *s* locations to be one quarter of a $\lambda_0 / 2$ fringe spacing (i.e., $\lambda_0 / 8$), 90 degree phase difference is introduced in the photo detector output responses to beam power *W*. Comparing photo detector phase shifted outputs determines which is leading or lagging the other, hence, the instantaneous direction of integrated sensed angular rate.

The RLG photo detectors measure the effect of integrated angular rate in the forms of cyclic outputs each time the $\frac{2}{\lambda_0} \int_0^{t_{wav}} \left( \frac{dA_p}{dL_p} d\theta_{p_{Inpt}} + \frac{dA_q}{dL_q} d\theta_{q_{Inpt}} \right)$ term in (38) changes by 1. By triggering on the rising and falling edge of the equivalent square wave response generated in the readout electronics, four sequential digital output discretes ("pulses") are generated per cycle,

each indicating gyro rotation through a known angular increment. The output scale factor (micro-radians rotation per output pulse) for a particular RLG configuration depends on the number of mirrors defining the wave path, the relative mirror positioning around the wave path, and whether the mirror geometry defines a planar or non-planar waveguide configuration (discussed next).

Planar RLGs

Eq. (38) describes the general operation of an idealized RLG. The form of (38) simplifies for most RLGs in which the closed beam path lies in a plane, and in which the point *a* "rotation center" represents the "centroid" of the waveguide, a point that is equally distant along a line perpendicular to any leg (i.e., between any two mirrors) of the beam path. Such a condition would be met for a closed planar light path shaped as a circle (the classical hypothetical model commonly used for simplified analysis), any triangle, or any equal-sided tetrahedron having the same angle between any two sides (e.g., a square with 90 degrees between any two sides).

For a planar closed path configuration, RLG input axes $\underline{u}_{Inpt_p}$ , $\underline{u}_{Inpt_q}$ for the *p* and *q* photon motion detection of $d\underline{\theta}_{IB}$ will be the same, and the centroid-to-leg perpendicular distance for *p* photon motion is exactly $\left| \underline{x}_{p/a} \times \dfrac{d\underline{\chi}_{p/b}}{\left| d\underline{\chi}_{p/b} \right|} \right| = \left| \dfrac{\underline{x}_{p/a} \times d\underline{\chi}_{p/b}}{dL_p} \right| = 2\dfrac{dA_p}{dL_p}$ (and similarly for photon *q*). Thus, $\dfrac{dA_p}{dL_p}$ and $\dfrac{dA_q}{dL_q}$ in (38) will both be constant and equal (call it $\dfrac{dA}{dL}$), and $d\theta_{p_{Inpt}}$ in (38) will equal $d\theta_{q_{Inpt}}$ (call it $d\theta_{Inpt}$). Then (38) simplifies to

$$W = 1 + \cos 2\pi \left( \frac{2s}{\lambda_0} - \frac{\beta_p - \beta_q}{2\pi} + \frac{4}{\lambda_0} \frac{dA}{dL} \int_0^{t_{wav}} d\theta_{Inpt} \right) \tag{39}$$

Further refinement in (39) is achieved from the integral of $dA/dL$ with respect to the differential distance $dL$ over the length of the closed wave path:

$$\begin{aligned} \int_{L=0}^{L=L_{Pth}} \frac{dA}{dL} dL &= \int_{L=0}^{L=L_{Pth}} dA = A_{Pth} \\ \int_{L=0}^{L=L_{Pth}} \frac{dA}{dL} dL &= \frac{dA}{dL} \int_{L=0}^{L=L_{Pth}} dL = \frac{dA}{dL} L_{Pth} \end{aligned} \tag{40}$$

where $A_{Pth}$ is the area enclosed by photon as it traverses the closed optical path and $L_{Pth}$ is the closed optical path perimeter. Equating the two expressions in (40) shows that

$$\frac{dA}{dL} = \frac{A_{Pth}}{L_{Pth}} \tag{41}$$

With (41), (39) assumes the more commonly recognized "area-to-perimeter-ratio" coefficient form

$$W = 1 + \cos 2\pi \left( \frac{2s}{\lambda_0} - \frac{\beta_p - \beta_q}{2\pi} + \frac{4}{\lambda_0} \frac{A_{Pth}}{L_{Pth}} \int_0^{t_{wav}} d\theta_{Inpt} \right) \tag{42}$$

The photo detector response to the (42) input generates a cyclic output that repeats each time $\frac{4}{\lambda_0} \frac{A_{Pth}}{L_{Pth}} \int_0^{t_{wav}} d\theta_{Inpt}$ changes by 1, corresponding to an output "scale factor" of $1 / \left( \frac{4}{\lambda_0} \frac{A_{Pth}}{L_{Pth}} \right)$ radians change in $\int_0^{t_{wav}} d\theta_{Inpt}$ per photo detector output cycle. For an equilateral triangular RLG with each side having length *S*, $A_{Pth} = (S/2) \frac{\sqrt{3}}{2} S = \frac{\sqrt{3}}{4} S^2$, $L_{Pth} = 3S$, and $\frac{A_{Pth}}{L_{Prmtr}} = \frac{\sqrt{3}}{12} S$. For *S* = 4.2 inches = 0.35 ft and the commonly used visible RLG wavelength $\lambda_0$ = 0.63 micron = 2.02 e-6 ft, the photo detector output scale factor will be

$$1 / \left( \frac{4}{\lambda_0} \frac{A_{Pth}}{L_{Pth}} \right) = 1 / \left( \frac{4}{2.02e-6} \frac{\sqrt{3}}{12} 0.35 \right) = 1.00\, e-5 \text{ radians} = 2.06 \text{ arc sec per output cycle}$$

By triggering 2 pulse outputs from each of the two photo detectors (being position phased in quadrature - 90 degrees apart as described previously), the combined output pulse scale factor would be 2.06 / 4 = 0.515 arc sec per pulse.

A square RLG configuration would have $A_{Pth} = S^2$, $L_{Pth} = 4S$, and $\frac{A_{Pth}}{L_{Pth}} = \frac{1}{4} S$. For a scale factor equivalent to the previously described 4.2 inch per side triangular RLG, the square RLG would have $1 / \left( \frac{4}{\lambda_0} \frac{A_{Pth}}{L_{Pth}} \right) = 1 / \left( \frac{4}{2.02e-6} \frac{1}{4} S \right) = \frac{2.02e-6}{S} = 1.00\, e-5$ for which $S = 0.202$ ft = 2.42 inches and $L_{Pth} = 4S = 9.68$ inches = 24.6 centimeters.

Non-Planar RLGs

For RLGs in which the closed wave path does not lie in a single plane (due to intentional alignment of the reflecting mirrors [12]), an equivalent to (42) can be derived from a revised form of (38) where the integral term is defined to be a sum of integrals, each over the time interval $T_{Pth}$ for a photon to traverse the closed waveguide optical path relative to the gyro:

$$\int_0^{t_{wav}} \left( \frac{dA_p}{dL_p} d\theta_{p_{Inpt}} + \frac{dA_q}{dL_q} d\theta_{q_{Inpt}} \right) = \sum_{i=1,n} \int_0^{T_{Pth}} \left( \frac{dA_p}{dL_p} d\theta_{p_{Inpt}} + \frac{dA_q}{dL_q} d\theta_{q_{Inpt}} \right) \quad (43)$$

where $n$ is the total number of $i$ circuits traversed around the waveguide for photons $p$ and $q$ relative to the rotating gyro. Recognizing that the photons are travelling relative to the gyro at the speed of light, photon $p$ will traverse an incremental distance $dL_p = c\,dt$ at point $b$ on the waveguide during time interval $dt$. Thus, the $p$ photon path integrand in (43) expands as

$$\frac{dA_p}{dL_p} d\theta_{p_{Inpt}} = \frac{dA_p}{dL_p} \underline{u}_{Inpt_p} \cdot d\underline{\theta}_{IB} = \frac{d\underline{A}_{Inpt_p}}{dL_p} \cdot d\underline{\theta}_{IB} = d\underline{A}_{Inpt_p} \cdot \frac{d\underline{\theta}_{IB}}{dL_p} = d\underline{A}_{Inpt_p} \cdot \frac{d\underline{\theta}_{IB}}{c\,dt} \quad (44)$$

where $d\underline{A}_{Inpt_p}$ is the vectorial area vector traversed by photon $p$ during $dt$. For $d\underline{\theta}_{IB}/dt$ approximated to be constant over the time for $p$ to traverse the closed waveguide, the $p$ integral in (43) with (44) approximates as

$$\begin{aligned} \int_0^{T_{Pth}} \frac{dA_p}{dL_p} d\theta_{p_{Inpt}} &= \int_0^{T_{Pth}} d\underline{A}_{Inpt_p} \cdot \frac{d\underline{\theta}_{IB}}{c\,dt} \approx \left( \int_0^{T_{Pth}} d\underline{A}_{Inpt_p} \right) \cdot \frac{d\underline{\theta}_{IB}}{c\,dt} \\ &\approx \left( \int_0^{T_{Pth}} d\underline{A}_{Inpt_p} \right) \cdot \frac{\Delta\underline{\theta}_{IB_i}}{c\,T_{Pth}} = \frac{\left( \int_0^{T_{Pth}} d\underline{A}_{Inpt_p} \right)}{L_{Pth}} \cdot \Delta\underline{\theta}_{IB_i} \end{aligned} \quad (45)$$

where $\Delta\underline{\theta}_{IB_i}$ is the angular rotation of the gyro over the time interval $T_{Pth}$ for the $i^{\text{th}}$ circuit of $p$ around the waveguide, and as before, $L_{Pth}$ is the distance travelled by photon $p$ around the wave path. We then define

$$\left( \frac{A_{Pth}}{L_{Pth}} \right)_{pAvg} \equiv \frac{\left| \int_0^{T_{Pth}} d\underline{A}_{Inpt_p} \right|}{L_{Pth}} \qquad \underline{u}_{Inpt_{pAvg}} \equiv \frac{\int_0^{T_{Pth}} d\underline{A}_{Inpt_p}}{\left| \int_0^{T_{Pth}} d\underline{A}_{Inpt_p} \right|}$$

$$\therefore \quad \frac{\left( \int_0^{T_{Pth}} d\underline{A}_{Inpt_p} \right)}{L_{Pth}} = \left( \frac{A_{Pth}}{L_{Pth}} \right)_{pAvg} \underline{u}_{Inpt_{pAvg}} \quad (46)$$

where $\left( \frac{A_{Pth}}{L_{Pth}} \right)_{pAvg}$ is the average area to perimeter ratio for $p$ photon motion (analogous to $\frac{A_{Pth}}{L_{Pth}}$ in (42) for the planar RLG), and $\underline{u}_{Inpt_{pAvg}}$ is the corresponding average input axis for $\Delta\underline{\theta}_{IB_i}$ sensing. With (46), (45) becomes

$$\int_0^{TPth} \frac{dA_p}{dL_p} d\theta_{p_{Inpt}} = \left(\frac{A_{Pth}}{L_{Prmtr}}\right)_{pAvg} \underline{u}_{Inpt_{pAvg}} \cdot \Delta\underline{\theta}_{IB_i} = \left(\frac{A_{Pth}}{L_{Prmtr}}\right)_{pAvg} \Delta\theta_{pInpt_i} \quad (47)$$

where $\Delta\theta_{pInpt_i}$ is the component of $\Delta\underline{\theta}_{IB_i}$ along $\underline{u}_{Inpt_{pAvg}}$ . The $p$ summation in (43) then becomes

$$\begin{aligned} \sum_{i=1,n} \int_0^{TPth} \frac{dA_p}{dL_p} d\theta_{p_{Inpt}} &= \sum_{i=1,n} \left[ \left(\frac{A_{Pth}}{L_{Pth}}\right)_{pAvg} \Delta\theta_{pInpt_i} \right] \\ = \left(\frac{A_{Pth}}{L_{Pth}}\right)_{pAvg} \sum_{i=1,n} \Delta\theta_{pInpt_i} &= \left(\frac{A_{Pth}}{L_{Pth}}\right)_{pAvg} \int_0^{t_{wav}} d\theta_{p_{Inpt}} \end{aligned} \quad (48)$$

Since the $p$ and $q$ waves traverse the same closed path at the speed of light over the same time period, the identical (48) result is obtained for the $q$ photon:

$$\begin{aligned} \sum_{i=1,n} \int_0^{TPth} \frac{dA_q}{dL_q} d\theta_{q_{Inpt}} &= \sum_{i=1,n} \int_0^{TPth} \frac{dA_p}{dL_p} d\theta_{p_{Inpt}} \\ = \left(\frac{A_{Pth}}{L_{Pth}}\right)_{pAvg} \int_0^{t_{wav}} d\theta_{p_{Inpt}} &= \left(\frac{A_{Pth}}{L_{Pth}}\right)_{Avg} \int_0^{t_{wav}} d\theta_{Inpt} \end{aligned} \quad (49)$$

in which the more general form of (46) is used for $\left(\frac{A_{Pth}}{L_{Pth}}\right)_{Avg}$ and $d\theta_{Inpt}$ definition:

$$\frac{\int_0^{TPth} d\underline{A}_{Inpt}}{L_{Pth}} = \left(\frac{A_{Pth}}{L_{Pth}}\right)_{Avg} \underline{u}_{Inpt_{Avg}} \qquad d\theta_{Inpt} \equiv \underline{u}_{Inpt_{Avg}} \cdot d\underline{\theta}_{IB} \quad (50)$$

With (49), (43) becomes

$$\begin{aligned} \int_0^{t_{wav}} \left( \frac{dA_p}{dL_p} d\theta_{p_{Inpt}} + \frac{dA_q}{dL_q} d\theta_{q_{Inpt}} \right) &= \sum_{i=1,n} \int_0^{T_{Pth}} \left( \frac{dA_p}{dL_p} d\theta_{p_{Inpt}} + \frac{dA_q}{dL_q} d\theta_{q_{Inpt}} \right) \\ &= 2 \left(\frac{A_{Pth}}{L_{Prmtr}}\right)_{Avg} \int_0^{t_{wav}} d\theta_{Inpt} \end{aligned} \quad (51)$$

Substituting (51) in (38) then gives for the non-planar RLG:

$$W = 1 + \cos 2\pi \left[ \frac{2s}{\lambda_0} - \frac{\beta_p - \beta_q}{2\pi} + \frac{4}{\lambda_0} \left(\frac{A_{Pth}}{L_{Pth}}\right)_{Avg} \int_0^{t_{wav}} d\theta_{Inpt} \right] \quad (52)$$

which is identical to (42) for the planar RLG when $\left(\frac{A_{Pth}}{L_{Pth}}\right)_{Avg}$ is substituted for $\frac{A_{Pth}}{L_{Pth}}$.

When analytically evaluating $\left(\frac{A_{Pth}}{L_{Pth}}\right)_{Avg}$ for a particular RLG non-planar geometry, it is convenient to define $\int_0^{L_{Pth}} d\underline{A}_{Inpt}$ in the (50) definitions in terms of differential position parameters during a circuit around the wave path. Thus, based on Fig. 2, over the total wave path distance $L_{Pth}$ for photon travel:

$$\int_0^{L_{Pth}} d\underline{A}_{Inpt} = \frac{1}{2}\int_0^{L_{Pth}} \underline{x}_{p/a} \times d\underline{\chi}_p \tag{53}$$

where $d\underline{\chi}_p$ is now defined as a differential distance vector at point *p* along the waveguide, $\underline{x}_{p/a}$ is the distance vector from an arbitrary reference point *a* in the gyro to point *p*, and the integral is around the wave path.

## FIBER-OPTIC GYROS

A fiber optic gyro (FOG) consists of a circular coil of optical fiber, the ends optically spliced together with fiber-optic couplers that route near monochromatic light from a super-luminescent diode (e.g., gallium arsenide) into and out of the coil [13 pp 186-190; 14; 15]. The concept is depicted in Fig. 5.

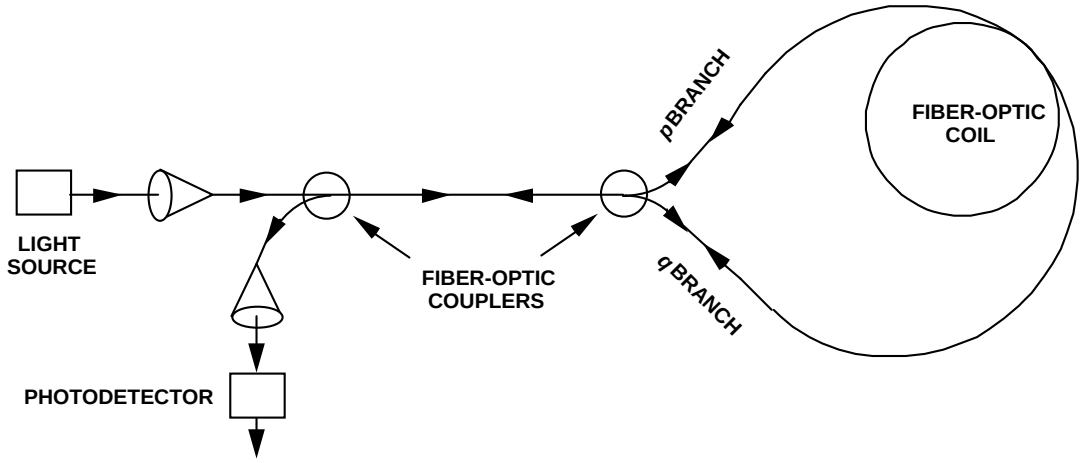


Fig. 5 - Fiber Optic Gyro (FOG) Concept

The light beam from the photo diode light source in Fig. 5 passes through a first coupler, then into the fiber-coil through a second coupler where it is split into two beams, one identified as the *p* branch, the other oppositely directed into the *q* branch. After traversing the coil, the beams recombine in the second coupler, and are gated through the first coupler to a readout photo detector. Under rotation, the *p* and *q* branch beams experience a relative phase shift, generating a change in the combined beam power illuminating the photo detector. Readout electronics convert the photo detector output into a measurement of angular rotation that created the phase shift.

Fundamental FOG Analytical Model

As with the RLG, the fundamental operation of a FOG can be represented by (37), describing the continuous light wave emitted from the diode light source in Fig. 5. The basic difference in fiber optic and ring laser gyro operation is that for a FOG, each photon traverses the waveguide once from its photo-diode light source to the pickoff. In contrast, photons in an RLG traverse the waveguide continually. Thus, in an RLG, the $t_{wav}$ time interval in (37) represents the current time since gyro turn-on whereas in a FOG, $t_{wav}$ represents the time interval $T_{Pth}$ for a photon to reach the pickoff after once traversing the optical fiber wave path. Since the counter-travelling photons in a FOG originate from the same source, they enter the waveguide at the same phase $\alpha$, thereby setting $\beta_P + \beta_q$ in (37) to $2\alpha$ and $\beta_P - \beta_q$ to zero. Since there is only one pickoff in a FOG, we can define the *s* waveguide reference point in (37) as the photo detector location, thereby equating *s* to zero. For the Fig. 5 FOG configuration, the general (37) analytical power model then simplifies to

$$W = \left\{1 - \cos\left[\frac{4\pi c\, T_{Pth}}{\lambda_0} + 2\alpha - \frac{4\pi}{\lambda_0}\int_0^{T_{Pth}} \left(\frac{dA_p}{dL_p}\, d\theta_{p\,Inpt} - \frac{dA_q}{dL_q}\, d\theta_{q\,Inpt}\right)\right]\right\} \times \left\{1 + \cos\left[\frac{4\pi}{\lambda_0}\int_0^{T_{Pth}} \left(\frac{dA_p}{dL_p}\, d\theta_{p\,Inpt} + \frac{dA_q}{dL_q}\, d\theta_{q\,Inpt}\right)\right]\right\} \quad (54)$$

For the RLG, the equivalent to $\frac{4\pi c\, T_{Pth}}{\lambda_0} + 2\alpha$ in (54) was $\frac{4\pi c}{\lambda_0} t_{wav} + \beta_p + \beta_q$ in (37). For the RLG it was shown in the paragraph leading from (37) to (38), that $\frac{2c}{\lambda_0}$ was high enough in frequency (i.e., 9.52 e14 Hz) that the associated cosine term would be attenuated by the readout electronics. For a FOG, however, the $\frac{2c}{\lambda_0}$ frequency in (54) does not produce cosine term attenuation because it multiplies a fixed time interval $T_{Pth}$ rather than running time $t_{wav}$.

On the other hand, the $\beta_p + \beta_q$ term in (37) is constant for an RLG (by virtue of the laser stimulation emission feedback process), but the corresponding $2\alpha$ term in (54) for the FOG is

continually changing at high frequency. The reason is that in (54), $\alpha$ represents phase shift imparted to a light wave when it entered the waveguide, which then propagates at that value to the readout photo detector. At a time instant *dt* later, another wave will reach the readout with a different $\alpha$ value because it entered the waveguide *dt* later than the previous wave. Because the waves are generated continuously by the photo diode light source, the $\alpha$ phase of waves entering the waveguide (at the speed of light *c* with approximate wavelength $\lambda_0$) will be continuously changing at $\frac{2\pi c}{\lambda_0}$ Hz, producing a corresponding $2\alpha$ change rate of $\frac{4\pi c}{\lambda_0}$. Over time, the $2\alpha$ value at the readout will then also be changing at $\frac{4\pi c}{\lambda_0}$. This is exactly the same change rate as for the $\frac{4\pi c}{\lambda_0} t_{wav}$ term in (37) whose associated cosine term was attenuated in an RLG by the readout electronics, leading to (38). Thus, $2\alpha$ in (54) will also cause its cosine term to be attenuated in the FOG readout electronics, thereby simplifying (54) to

$$W = 1 + \cos \frac{4\pi}{\lambda_0} \int_0^{T\,Pth} \left( \frac{dA_p}{dL_p} d\theta_{p\,Inpt} + \frac{dA_q}{dL_q} d\theta_{q\,Inpt} \right) \tag{55}$$

Eq. (55) describes the general operation of a FOG. As with the non-planar geometry RLG, (55) can now be formulated to show a more specific relationship for a particular FOG optical fiber winding geometry.

Following the same reasoning leading to (52) for the non-planar RLG, recognize for the FOG that photons are also travelling relative to the gyro at the speed of light, hence, photon *p* will traverse an incremental distance $dL_p = c\,dt$ at point *b* on the fiber coil during time interval $dt$. The *p* photon path integral in (55) thereby expands as

$$\frac{dA_p}{dL_p} d\theta_{p\,Inpt} = \frac{dA_p}{dL_p} \underline{u}_{Inpt_p} \cdot d\underline{\theta}_{IB} = \frac{d\underline{A}_{Inpt\,p}}{dL_p} \cdot d\underline{\theta}_{IB} = d\underline{A}_{Inpt_p} \cdot \frac{d\underline{\theta}_{IB}}{dL_p} = d\underline{A}_{Inpt_p} \cdot \frac{d\underline{\theta}_{IB}}{c\,dt} \tag{56}$$

where $d\underline{A}_{Inpt_p}$ is the vectorial area vector traversed by photon *p* during $dt$. For $d\underline{\theta}_{IB}/dt$ approximated as constant over the time for *p* to traverse the fiber coil, the *p* integral in (55) approximates as

$$\begin{aligned} \int_0^{TPth} \frac{dA_p}{dL_p} d\theta_{p\,Inpt} &= \int_0^{TPth} d\underline{A}_{Inpt\,p} \cdot \frac{d\underline{\theta}_{IB}}{c\,dt} \approx \left( \int_0^{TPth} d\underline{A}_{Inpt\,p} \right) \cdot \frac{d\underline{\theta}_{IB}}{c\,dt} \\ &\approx \left( \int_0^{T\,Pth} d\underline{A}_{Inpt_p} \right) \cdot \frac{\Delta\underline{\theta}_{IB}}{c\,T_{Pth}} = \frac{\left( \int_0^{TPth} d\underline{A}_{Inpt_p} \right)}{L_{Pth}} \cdot \Delta\underline{\theta}_{IB} \end{aligned} \tag{57}$$

where (as for the non-planar RLG) $\Delta\underline{\theta}_{IB}$ is the angular rotation of the gyro over the $T_{Pth}$ time interval, and $L_{Pth}$ is the length of the fiber coil. We then define

$$\left(\frac{A_{Pth}}{L_{Pth}}\right)_{pAvg} \equiv \frac{\left|\int_0^{T_{Pth}} d\underline{A}_{Inpt_p}\right|}{L_{Pth}} \qquad \underline{u}_{Inpt_{pAvg}} \equiv \frac{\int_0^{T_{Pth}} d\underline{A}_{Inpt_p}}{\left|\int_0^{T_{Pth}} d\underline{A}_{Inpt_p}\right|} \tag{58}$$

$$\therefore \quad \frac{\left(\int_0^{T_{Pth}} d\underline{A}_{Inpt_p}\right)}{L_{Pth}} = \left(\frac{A_{Pth}}{L_{Pth}}\right)_{pAvg} \underline{u}_{Inpt_{pAvg}}$$

where $\left(\frac{A_{Pth}}{L_{Pth}}\right)_{pAvg}$ is the average area to coil length ratio for *p* photon motion as in (46) for the non-planar RLG), and $\underline{u}_{Inpt_{pAvg}}$ is the corresponding average input axis for $\Delta\underline{\theta}_{IB}$ angular increment sensing. With (58), (57) becomes

$$\int_0^{T_{Pth}} \frac{dA_p}{dL_p} d\theta_{p_{Inpt}} = \left(\frac{A_{Pth}}{L_{Pth}}\right)_{pAvg} \underline{u}_{Inpt_{pAvg}} \cdot \Delta\underline{\theta}_{IB} = \left(\frac{A_{Pth}}{L_{Pth}}\right)_{pAvg} \Delta\theta_{p_{Inpt}} \tag{59}$$

where $\Delta\theta_{p_{Inpt}}$ is the component of $\Delta\underline{\theta}_{IB}$ along $\underline{u}_{Inpt_{pAvg}}$.

Since the *p* and *q* waves traverse the same closed path at the speed of light over the same time period, the identical (59) result is obtained for the *q* photon:

$$\int_0^{T_{Pth}} \frac{dA_q}{dL_q} d\theta_{q_{Inpt}} = \int_0^{T_{Pth}} \frac{dA_p}{dL_p} d\theta_{p_{Inpt}} = \left(\frac{A_{Pth}}{L_{Pth}}\right)_{pAvg} \Delta\theta_{p_{Inpt}} = \left(\frac{A_{Pth}}{L_{Pth}}\right)_{Avg} \Delta\theta_{Inpt} \tag{60}$$

in which the more general form is now used for $\left(\frac{A_{Pth}}{L_{Pth}}\right)_{Avg}$ and $\Delta\theta_{Inpt}$ definition:

$$\left(\frac{A_{Pth}}{L_{Pth}}\right)_{Avg} \equiv \frac{\left|\int_0^{T_{Pth}} d\underline{A}_{Inpt}\right|}{L_{Pth}} \qquad \underline{u}_{Inpt_{Avg}} \equiv \frac{\int_0^{T_{Pth}} d\underline{A}_{Inpt}}{\left|\int_0^{T_{Pth}} d\underline{A}_{Inpt}\right|} \tag{61}$$

$$\frac{\int_0^{T_{Pth}} d\underline{A}_{Inpt}}{L_{Pth}} = \left(\frac{A_{Pth}}{L_{Pth}}\right)_{Avg} \underline{u}_{Inpt_{Avg}} \qquad \Delta\theta_{Inpt} \equiv \underline{u}_{Inpt_{Avg}} \cdot \Delta\underline{\theta}_{IB}$$

With (60), (55) becomes for FOG optical power impinging in Fig. 5 on the readout photo detector:

$$W = 1 + \cos\Delta\phi \qquad \Delta\phi \equiv \frac{8\pi}{\lambda_0}\left(\frac{A_{Pth}}{L_{Pth}}\right)_{Avg} \Delta\theta_{Inpt} \tag{62}$$

where $\Delta\phi$ is the scaled angular rotation $\Delta\theta_{Inpt}$ having scale factor $\frac{8\pi}{\lambda_0}\left(\frac{A_{Pth}}{L_{Pth}}\right)_{Avg}$.

When evaluating $\left(\frac{A_{Pth}}{L_{Pth}}\right)_{Avg}$ in (62) for a particular FOG fiber coil winding geometry, it is more convenient to define $\int_0^{TPth} d\underline{A}_{Inpt}$ in the (61) definitions in terms of differential position parameters along the fiber coil. Thus, similar to (53) and Fig. 2 for the RLG, over the total fiber coil length $L_{Pth}$ for photon travel:

$$\int_0^{TPth} d\underline{A}_{Inpt} = \frac{1}{2}\int_0^{LPth} \underline{x}_{p/a} \times d\underline{\chi}_p \tag{63}$$

where $d\underline{\chi}_p$ is now defined as a differential distance vector at point *p* along the fiber coil, $\underline{x}_{p/a}$ is the distance vector from an arbitrary reference point *a* in the FOG to point *p*, and the integral is over the total $L_{Pth}$ fiber coil length.

A more commonly represented form for $\Delta\phi$ in (62) is derived from (61):

$$\begin{aligned}\Delta\phi = \frac{8\pi}{\lambda_0}\left(\frac{A_{Pth}}{L_{Pth}}\right)_{Avg}\Delta\theta_{Inpt} &= \frac{8\pi}{\lambda_0}\frac{\left|\int_0^{TPth} d\underline{A}_{Inpt}\right|}{L_{Pth}}\Delta\theta_{Inpt} = \frac{8\pi}{\lambda_0}\frac{\left|\int_0^{TPth} d\underline{A}_{Inpt}\right|}{c\,T_{Pth}}\Delta\theta_{Inpt} \\ &= \frac{8\pi}{c\,\lambda_0}\left|\int_0^{TPth} d\underline{A}_{Inpt}\right|\frac{\Delta\theta_{Inpt}}{T_{Pth}} \approx \frac{8\pi\left|\int_0^{TPth} d\underline{A}_{Inpt}\right|}{c\,\lambda_0}\frac{d\theta_{Inpt}}{dt}\end{aligned} \tag{64}$$

If the fiber coil is then approximated as a connected set of parallel overlapping circular segments, $\left|\int_0^{TPth} d\underline{A}_{Inpt}\right| = n\,A$ where $A$ is the area of each circular segment and $n$ is the number of segments in the coil. For each segment having a 3 inch diameter and a fiber length $L_{Pth}$ of 1000 meters, there are 1000 / (0.0254 × 3 $\pi$) ≈ 4,177 circular segments ($n$), each having an area $A$ of $\pi\,(0.0254 \times 3 / 2)^2$ = 0.00456 meters-squared. Hence, $\left|\int_0^{TPth} d\underline{A}_{Inpt}\right| = n\,A$ = 4,177 × 0.00456 = 19.05 meters-squared. For an angular rate $d\theta_{Inpt}/dt$ of 7 rad/sec (approximately 400

deg/sec) and a light source wavelength $\lambda_0$ of 0.82 microns (for a gallium-arsenide photo-diode), the phase difference $\Delta\phi$ in (64) induced at the FOG pickoff will be [8 $\pi$ × 19.05 / (3.0e8 × 0.82e-6)] × 7 = 13.6 rad.

To be useful for computing angular orientation in system applications, it is important that FOG output measurements of $\Delta\theta_{Inpt}$ in (63) represent successive increments of angular change. Then, using simultaneous outputs from three orthogonally mounted FOGs, they can be used effectively in an appropriate computation algorithm for repetitive three-dimensional attitude computation updating. Since each measurement of $\Delta\phi$ in (62) represents an attitude change over $T_{Pth}$ (the time for a photon to traverse the optical fiber coil), this means that $\Delta\phi$ measurements must be sampled and output at a frequency of $1/T_{Pth}$. For $T_{Pth}$ on the order of 1 micro sec (typical) and 1000 meters of optical fiber in the coil, this translates into a $\Delta\phi$ measurement/sampling rate 3.0e8 meters/sec (the speed of light) divided by 1000 meters = 0.3 mega Hz. For contrast, an RLG with a 0.515 arc sec output pulse size has an output pulse rate at 400 deg/sec rotation rate of 400 × 3,600 arc sec per deg / 0.515 = 2.8 mega Hz.

"Closed-Loop" FOG Configuration

A significant difference between the RLG and FOG arises in the complexity of the readout implementation. Most high accuracy mechanical gyros have been implemented in the past using narrow angle pickoffs designed to operate over a small angular input range (e.g., 1 milli-rad). The purpose is to minimize the effect of pickoff scale factor error on device performance, and is typically achieved by controlling the pickoff output in servo feedback fashion to dynamically maintain the pickoff output (hence, pickoff input) at zero (null). This has been achieved by either mechanically controlling the base to which the gyro is mounted (i.e., with a mechanical gimbaled platform), or by using an electrical "closed-loop" rebalance whereby an electrical signal is generated from the pickoff output to provide angular rate bias feedback within the gyro to maintain pickoff null [16]. A closed-loop gyro output would then be generated within the rebalance loop from the biasing signal required to maintain pickoff null, thus becoming equal but opposite to the gyro dynamic angular input.

Eq. (62) illustrates the fundamental difficulty of measuring the scaled angular increment $\Delta\phi$ for an "open-loop" FOG; the lack of sensitivity in power $W$ for small $\Delta\phi$, becoming indeterminate at zero input rate, and prone to significant scale factor error (from pickoff output non-linearity characteristics) at non-zero angular increments. For a closed-loop FOG, the goal is to create closed-loop electrical bias that maintains $W$ at a known average value with high sensitivity for any value of $\Delta\phi$. Thus, means must be introduced to enable measuring deviations from the specified average $W$ beam power, and providing "closed loop" feedback to maintain $W$ at its specified average under all dynamic angular rate conditions.

For a closed–loop FOG, the equivalent to (62) also derives from (37), but with $\beta_p$ and $\beta_q$ including additional bias introduced within the fiber coil to enable closed-loop operation and $\Delta\phi$

determination under any input condition. Thus, in (37), $\beta_p = \alpha + \Delta\beta_p$ and $\beta_q = \alpha + \Delta\beta_q$ where $\alpha$ is the phase of the light beam entering the coil (splitting into *p* and *q* branches as in Fig. 5), and $\Delta\beta_p$, $\Delta\beta_q$ represent additional phase biases intentionally introduced within the coil. The closed-loop equivalent to (62) then derives from (37) using the same rationale that led to (62):

$$
\begin{aligned}
W &= \left\{1-\cos\left[\frac{4\pi c\, T_{Pth}}{\lambda_0}+\beta_p+\beta_q-\frac{4\pi}{\lambda_0}\int_0^{T_{Pth}}\left(\frac{dA_p}{dL_p}\,d\theta_{p\,Inpt}-\frac{dA_q}{dL_q}\,d\theta_{q\,Inpt}\right)\right]\right\}\times \\
&\quad \left\{1+\cos\left[-\left(\beta_p-\beta_q\right)+\frac{4\pi}{\lambda_0}\int_0^{T_{Pth}}\left(\frac{dA_p}{dL_p}\,d\theta_{p\,Inpt}+\frac{dA_q}{dL_q}\,d\theta_{q\,Inpt}\right)\right]\right\} \\
&= \left\{1-\cos\left[\frac{4\pi c\, T_{Pth}}{\lambda_0}+\left(\alpha+\Delta\beta_p\right)+\left(\alpha+\Delta\beta_q\right)-\frac{4\pi}{\lambda_0}\int_0^{T_{Pth}}\left(\frac{dA_p}{dL_p}\,d\theta_{p\,Inpt}-\frac{dA_q}{dL_q}\,d\theta_{q\,Inpt}\right)\right]\right\}\times \\
&\quad \left\{1+\cos\left[\left(\alpha+\Delta\beta_q\right)-\left(\alpha+\Delta\beta_p\right)+\frac{4\pi}{\lambda_0}\int_0^{T_{Pth}}\left(\frac{dA_p}{dL_p}\,d\theta_{p\,Inpt}+\frac{dA_q}{dL_q}\,d\theta_{q\,Inpt}\right)\right]\right\} \\
&= \left\{1-\cos\left[\frac{4\pi c\, T_{Pth}}{\lambda_0}+2\alpha+\Delta\beta_p+\Delta\beta_q-\frac{4\pi}{\lambda_0}\int_0^{T_{Pth}}\left(\frac{dA_p}{dL_p}\,d\theta_{p\,Inpt}-\frac{dA_q}{dL_q}\,d\theta_{q\,Inpt}\right)\right]\right\}\times \\
&\quad \left\{1+\cos\left[-\left(\Delta\beta_p-\Delta\beta_q\right)+\frac{4\pi}{\lambda_0}\int_0^{T_{Pth}}\left(\frac{dA_p}{dL_p}\,d\theta_{p\,Inpt}+\frac{dA_q}{dL_q}\,d\theta_{q\,Inpt}\right)\right]\right\} \\
&\approx 1+\cos\left[-\left(\Delta\beta_p-\Delta\beta_q\right)+\frac{8\pi}{\lambda_0}\left(\frac{A_{Pth}}{L_{Pth}}\right)_{Avg}\Delta\theta_{Inpt}\right]
\end{aligned}
\tag{65}
$$

Using condensed nomenclature, (65) becomes

$$
W = 1+\cos\left[\Delta\phi-\left(\Delta\beta_p-\Delta\beta_q\right)\right] \qquad \Delta\phi \equiv k_{SF}\,\Delta\theta_{Inpt} \qquad k_{SF} \equiv \frac{8\pi}{\lambda_0}\left(\frac{A_{Pth}}{L_{Pth}}\right)_{Avg} \tag{66}
$$

where (61) and (63) define $\left(\frac{A_{Pth}}{L_{Pth}}\right)_{Avg}$ and $\Delta\theta_{Inpt}$ in (66).

The FOG scale factor $k_{SF}$ in (66) shows that for a $\Delta\theta_{Inpt}$ angular rotation during the time for a photon to traverse the fiber coil length $L_{Pth}$, there is a corresponding $\frac{8\pi}{\lambda_0}\left(\frac{A_{Pth}}{L_{Pth}}\right)_{Avg}$ shift in phase between the counter-travelling light waves reaching the readout photo detector. For

comparison, (42) show that for a planar RLG, there would be a $2\pi$ change in the phase difference between counter-travelling waves at the readout for each $\int_0^{t_{wav}} d\theta_{Inpt}$ integrated angular rate change of $\frac{4}{\lambda_0}\frac{A_{Pth}}{L_{Pth}}$, the equivalent of $\frac{4}{\lambda_0}\frac{A_{Pth}}{L_{Pth}}2\pi = \frac{8\pi}{\lambda_0}\frac{A_{Pth}}{L_{Pth}}$ phase change per radian of angular rotation. Thus, both the FOG and RLG measure angular rotation changes by the same scale factor.

In modern day FOGs, integrated optics inserts are used to generate the $\Delta\beta_p$ and $\Delta\beta_q$ applied phase shifts in (66). The approach is based on the use of active electro-optic crystals that change the index of refraction of light passing through, e.g., lithium-niobate [13 pp 189-190]. With this approach, an integrated optics insert is constructed from a crystal of lithium-niobate using titanium strips diffused on the surface to gate light waves through the crystal. Voltage applied across the crystal changes the index of refraction of light passing through, changing the speed of light waves propagating through the crystal, and thereby adding phase shift.

For a given applied voltage, the same phase shift will be added to waves entering from either side of the crystal, i.e., from the *p* and *q* wave directions in a FOG fiber coil. Achieving a net phase difference in (66) relies on the crystal being inserted at one end of the fiber to take advantage of the time interval difference for a *p* wave (for example) to reach the readout photo detector compared to the *q* wave. Thus, imagine a crystal inserted at the end of the coil where the *p* wave begins its journey. Then a voltage $V_1$ (corresponding to a $\beta_1$ phase shift) applied to the crystal at current time $t_1$ will shift the *p* wave phase by $\Delta\beta_p = \beta_1$, but this shift will not appear on the photo detector until *p* completes its passage around the coil at a later time $t_2$. Now consider a *q* wave that entered the coil with *p* at time $t_1$, but travelling in the opposite direction from *p* around the coil, does not pass through the crystal until time $t_2$. If $V_2$ is being applied to the crystal at time $t_2$ (with corresponding phase shift $\beta_2$), the *q* wave will be phase shifted by $\Delta\beta_q = \beta_2$ when it reaches the photo detector at $t_2$. The net result is that at time $t_2$, the *p* and *q* waves with phase shifts $\Delta\beta_p$ and $\Delta\beta_q$ will combine on the photo detector to generate a phase shift difference $\Delta\beta_p - \Delta\beta_q = \beta_1 - \beta_2$ in the (66) beam power, depending on the logic used in setting $V_1$ and $V_2$. An example of applying this concept is depicted in Fig. 6, a closed-loop FOG version of Fig. 5.

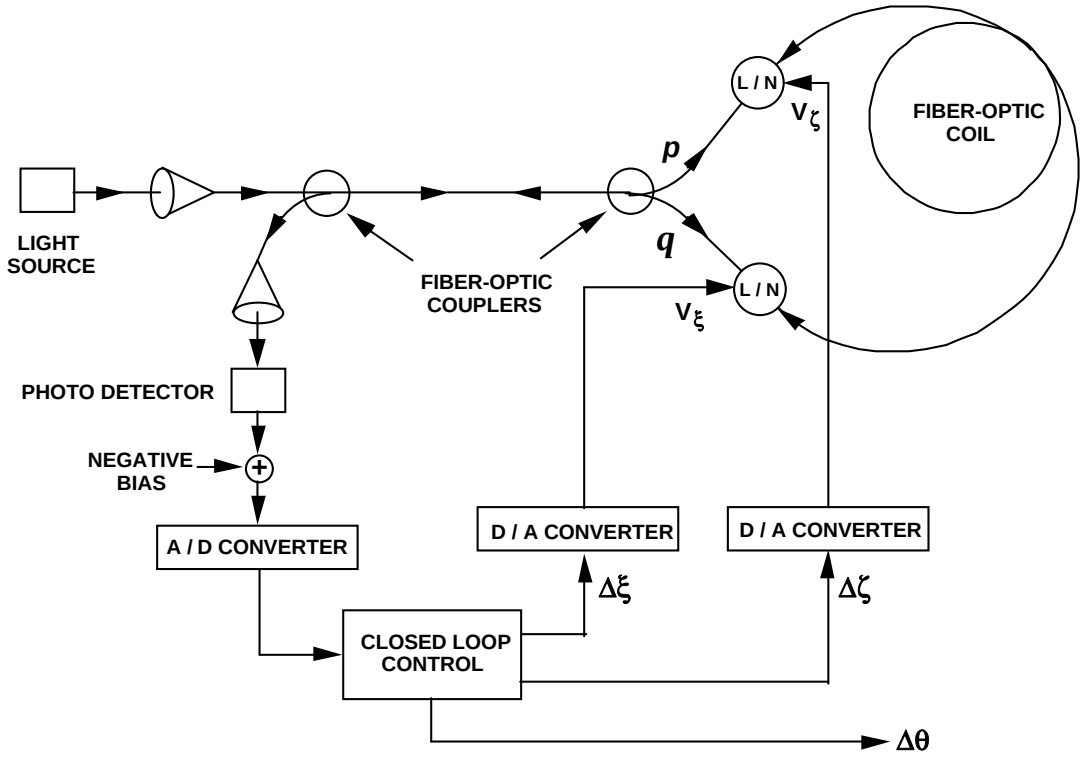


Fig. 6 – Closed-Loop FOG Configuration

A general goal in the design of inertial components is to provide symmetry to minimize the likelihood of asymmetric anomalous error generation. For a FOG, a symmetric design approach would use two lithium-niobate (L/N) crystals symmetrically placed in the *p* and *q* photon light paths at equal distances from the fiber coil junction, one located in the *p* branch, the other in the *q* branch. The symmetric configuration in Fig. 6 shows how the photo detector output would be applied in feedback fashion through the Closed Loop Control computation block to generate $\Delta\varsigma$, $\Delta\xi$ phase shifts in the *p*, *q* waves through $V_\varsigma$, $V_\xi$ voltages applied to the two L/N crystals. (The analog Negative Bias signal applied to the Analog-to-Digital (A/D) Converter input in Fig. 6 will be discussed later.) In conjunction with generating the $\Delta\varsigma$, $\Delta\xi$ phase shift commands, Closed Loop Control in Fig. 6 also computes $\Delta\theta$ angular increment measurements for output.

From (66) at time $t_i$, the combined *p* and *q* beam power illuminating the photo detector in Fig. 6 would be $W_i = 1 + \cos\left[\Delta\phi_i - \left(\Delta\beta_{p_i} - \Delta\beta_{q_i}\right)\right]$. The $\Delta\beta_{p_i}$ and $\Delta\beta_{q_i}$ phase shifts induced in $W_i$ as a function of the applied $\Delta\varsigma$, $\Delta\xi$ commands can be determined from Fig. 7 by following the progress of the $p$ and $q$ waves as they enter and leave the fiber coil.

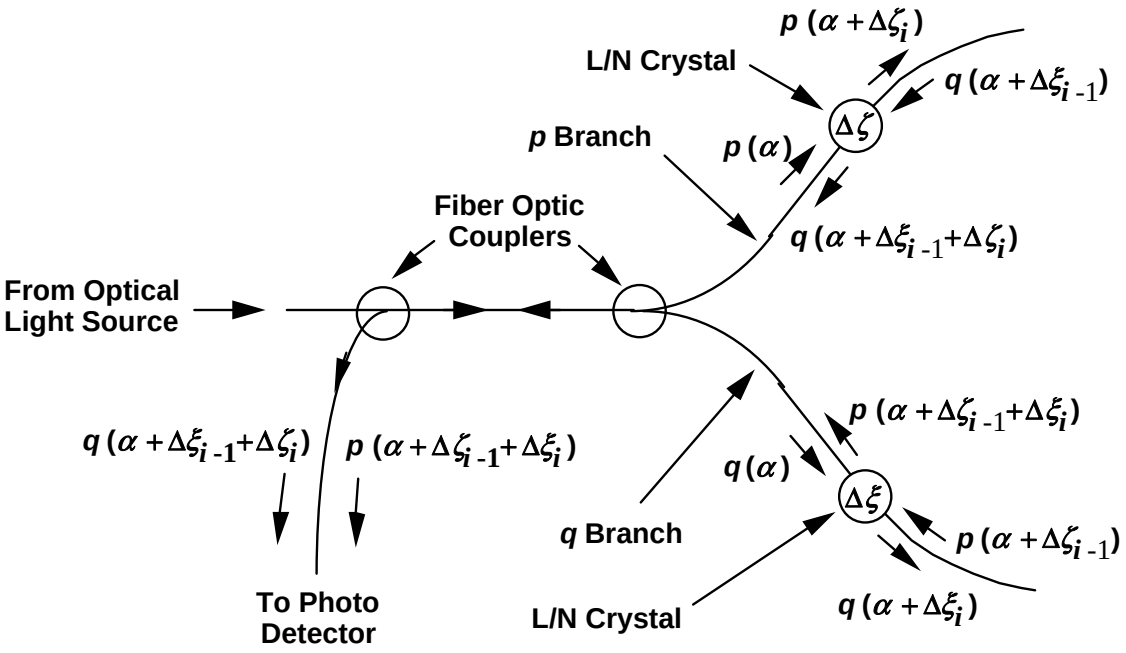


Fig. 7 – Closed-Loop FOG Signal Flow

At time $t_i$, a light wave at phase $\alpha$ from the Optical Light Source passes through the first coupler in Fig. 7, is gated into the fiber coil by the second coupler, then splits into *p* and *q* branches, each with phase $\alpha$ as denoted by $p(\alpha)$ and $q(\alpha)$. The *p* branch crystal imparts $\Delta\varsigma_i$ additional phase to the *p* wave at time $t_i$, generating $\alpha + \Delta\varsigma_i$ phase on the *p* output, denoted in Fig. 7 as $p(\alpha + \Delta\varsigma_i)$. Simultaneously at time $t_i$, a returning *q* wave at $q(\alpha + \Delta\xi_{i-1})$ (i.e., previously phase shifted by $\Delta\xi_{i-1}$ at $t_{i-1}$ by the *q* branch crystal) enters the *p* branch crystal, leaves at $q(\alpha + \Delta\xi_{i-1} + \Delta\varsigma_i)$, and is gated by the coupler to the readout Photo Detector. Thus, $\Delta\beta_{q_i}$ in (66), the shift in *q* wave phase from its $\alpha$ value at coil entry, will be $\Delta\beta_{q_i} = \Delta\xi_{i-1} + \Delta\varsigma_i$.

Similarly, the *q* branch crystal will impart $\Delta\xi_i$ additional phase to the *q* wave at time $t_i$, generating $q(\alpha + \Delta\xi_i)$ for the *q* output in Fig. 7. Simultaneously at time $t_i$, a returning *p* wave at $p(\alpha + \Delta\varsigma_{i-1})$ enters the *q* branch crystal, leaves at $p(\alpha + \Delta\varsigma_{i-1} + \Delta\xi_i)$, and is gated by the coupler to the readout photo detector. Thus, $\Delta\beta_{p_i}$ in (66), the shift in *p* wave phase from its $\alpha$ value at coil entry, will be $\Delta\beta_{p_i} = \Delta\varsigma_{i-1} + \Delta\xi_i$.

The net result is that at time $t_i$, the *p* and *q* waves will recombine as in (66) to have a total beam power input to the Fig. 7 photo detector of

$$W_i = 1+\cos\left[\Delta\phi_i - \left(\Delta\beta_{p_i} - \Delta\beta_{q_i}\right)\right] = 1+\cos\left\{\Delta\phi_i - \left[\left(\Delta\varsigma_{i-1}+\Delta\xi_i\right) - \left(\Delta\xi_{i-1}+\Delta\varsigma_i\right)\right]\right\}$$
$$= 1+\cos\left[\Delta\phi_i + \left(\Delta\varsigma_i - \Delta\varsigma_{i-1}\right) - \left(\Delta\xi_i - \Delta\xi_{i-1}\right)\right] \quad (67)$$

The $W_i$ photo detector measurement of (67) would be saved by Fig. 6 Closed Loop Control at time $t_i$. The $\Delta\varsigma_{i-1}$ and $\Delta\xi_{i-1}$ values in (67) would have been previously set during the time interval between $t_{i-2}$ to $t_{i-1}$, thus, generating the equivalent of (67) at time $t_{i-1}$ of

$$W_{i-1} = 1+\cos\left[\Delta\phi_{i-1} + \left(\Delta\varsigma_{i-1} - \Delta\varsigma_{i-2}\right) - \left(\Delta\xi_{i-1} - \Delta\xi_{i-2}\right)\right] \quad (68)$$

The $W_{i-1}$ photo detector measurement of (68) would have been saved in the Fig. 6 Closed Loop Control block at time $t_{i-1}$.

Between times $t_i$ and $t_{i+1}$, the $W_i$ readout from (67) (stored at time $t_i$) would be combined with $W_{i-1}$ from (68) (stored at time $t_{i-1}$) to calculate $\Delta\phi_i$ for output (between $t_i$ and $t_{i+1}$) and to maintain closed-loop control. The closed-loop control method selected depends on the analytical approach used in setting the $\Delta\varsigma$ s and $\Delta\xi$ s in (67) and (68). Examples are described next.

Examples of Closed-Loop FOG Control

Consider having the cosine function in (67) controlled to zero. Then the corresponding control law would be

$$\left(\Delta\varsigma_i - \Delta\varsigma_{i-1}\right) - \left(\Delta\xi_i - \Delta\xi_{i-1}\right) = -\widehat{\Delta\phi_i} \pm \pi/2 + 2\,n_i\,\pi \quad (69)$$

where $\widehat{\Delta\phi_i}$ is the control loop estimate for $\Delta\phi_i$ in (67) and $n_i$ is an arbitrary integer (to be subsequently chosen based on other considerations). With (69), and assuming that closed-loop operations maintain $\widehat{\Delta\phi_i} \approx \Delta\phi_i$, (67) becomes for cycle $i$:

$$W_i = 1+\cos\left[\Delta\phi_i + \left(\Delta\varsigma_i - \Delta\varsigma_{i-1}\right) - \left(\Delta\xi_i - \Delta\xi_{i-1}\right)\right]$$
$$= 1+\cos\left(\Delta\phi_i - \widehat{\Delta\phi_i} \pm \pi/2 + 2\,n_i\,\pi\right) = 1 \mp \sin\left(\Delta\phi_i - \widehat{\Delta\phi_i}\right) \quad (70)$$

In principle, (70) can be used to calculate $\Delta\phi_i$ using $\Delta\phi_i = \widehat{\Delta\phi_i} \pm \sin^{-1}(W_i - 1)$. This could be implemented for example, by applying the minus "1" as the Negative Bias signal in Fig. 6 to the photo detector output before sampling by the D/A converter. The problem with this approach

is that the "1" in (70) assumes accurate knowledge of normalizing scale factor $B^2$ in the (36) definition of normalized power $W$. To eliminate this error source, the minus option for the $\mp$ polarity in (70) is used for the $W_i$ measurement, and the plus option for the previous $W_{i-1}$ measurement. Then, similar to the (70) derivation from (68), the $W_{i-1}$ and $W_i$ measurements would become:

$$\begin{aligned} W_{i-1} &= 1+\cos\left[\Delta\phi_{i-1}+\left(\Delta\varsigma_{i-1}-\Delta\varsigma_{i-2}\right)-\left(\Delta\xi_{i-1}-\Delta\xi_{i-2}\right)\right] \\ &= 1+\cos\left(\Delta\phi_{i-1}-\widehat{\Delta\phi_{i-1}}+\pi/2+2\,n_{i-1}\,\pi\right)=1-\sin\left(\Delta\phi_{i-1}-\widehat{\Delta\phi_{i-1}}\right) \\ &= 1-\left(\Delta\phi_{i-1}-\widehat{\Delta\phi_{i-1}}\right)+\left(\Delta\phi_{i-1}-\widehat{\Delta\phi_{i-1}}\right)^3/6+\cdots \\ W_i &= 1+\cos\left[\Delta\phi_i+\left(\Delta\varsigma_i-\Delta\varsigma_{i-1}\right)-\left(\Delta\xi_i-\Delta\xi_{i-1}\right)\right] \\ &= 1+\cos\left(\Delta\phi_i-\widehat{\Delta\phi_i}-\pi/2+2\,n_i\,\pi\right)=1+\sin\left(\Delta\phi_i-\widehat{\Delta\phi_i}\right) \\ &= 1+\left(\Delta\phi_i-\widehat{\Delta\phi_i}\right)-\left(\Delta\phi_i-\widehat{\Delta\phi_i}\right)^3/6+\cdots \end{aligned} \tag{71}$$

Taking the difference between $W_i$ and $W_{i-1}$ cancels the "1", yielding

$$W_i-W_{i-1}=\left(\Delta\phi_i-\widehat{\Delta\phi_i}\right)+\left(\Delta\phi_{i-1}-\widehat{\Delta\phi_{i-1}}\right)-\left(\Delta\phi_i-\widehat{\Delta\phi_i}\right)^3/6-\left(\Delta\phi_{i-1}-\widehat{\Delta\phi_{i-1}}\right)^3/6+\cdots \tag{72}$$

which permits $\Delta\phi_i$ determination without "1" scale factor accuracy dependence:

$$\Delta\phi_i=\widehat{\Delta\phi_i}-\Delta\phi_{i-1}+\widehat{\Delta\phi_{i-1}}+\left(W_i-W_{i-1}\right)+\left(\Delta\phi_i-\widehat{\Delta\phi_i}\right)^3/6+\left(\Delta\phi_{i-1}-\widehat{\Delta\phi_{i-1}}\right)^3/6+\cdots \tag{73}$$

(Note in Fig. 6 that analog negative bias is applied to the photo detector output before sampling by the D/A converter. This generates a bias on the measured $W_i$ and $W_{i-1}$ signals in (73) which cancels when calculating $W_i-W_{i-1}$, including cancellation of error that may be present in the applied analog bias signal. This characteristic will be used subsequently to eliminate round-off error in closed-loop control operations.)

Finally, we assume that the $\Delta\phi$ increments will have very little change over the time interval for a photon to traverse the fiber coil so that $\Delta\phi_i\approx\Delta\phi_{i-1}$ and $\Delta\phi_{i-1}\approx\Delta\phi_{i-2}$. We can, therefore, set the $\widehat{\Delta\phi_i}$, $\widehat{\Delta\phi_{i-1}}$ estimates to

$$\widehat{\Delta\phi_i}=\Delta\phi_{i-1}\qquad\widehat{\Delta\phi_{i-1}}=\Delta\phi_{i-2} \tag{74}$$

Additionally, we assume that using $\widehat{\Delta\phi_i}$ from (74), the $\left(\Delta\phi_i - \widehat{\Delta\phi_i}\right)^3$ term in (73) will change very slowly from cycle to cycle so that

$$\left(\Delta\phi_i - \widehat{\Delta\phi_i}\right)^3 = \left(\Delta\phi_i - \Delta\phi_{i-1}\right)^3 \approx \left(\Delta\phi_{i-1} - \Delta\phi_{i-2}\right)^3 \tag{75}$$

With (74) and (75), Eqs. (71), (72), and (73) become

$$\begin{aligned} W_{i-1} &= 1 + \cos\left[\Delta\phi_{i-1} + \left(\Delta\varsigma_{i-1} - \Delta\varsigma_{i-2}\right) - \left(\Delta\xi_{i-1} - \Delta\xi_{i-2}\right)\right] \\ &= 1 + \cos\left(\Delta\phi_{i-1} - \Delta\phi_{i-2} + \pi/2 + 2\,n_{i-1}\,\pi\right) \\ W_i &= 1 + \cos\left[\Delta\phi_i + \left(\Delta\varsigma_i - \Delta\varsigma_{i-1}\right) - \left(\Delta\xi_i - \Delta\xi_{i-1}\right)\right] \\ &= 1 + \cos\left(\Delta\phi_i - \Delta\phi_{i-1} - \pi/2 + 2\,n_i\,\pi\right) \\ \Delta\phi_i &= \Delta\phi_{i-2} + \left(W_i - W_{i-1}\right) + \left(\Delta\phi_{i-1} - \Delta\phi_{i-2}\right)^3/3 \end{aligned} \tag{76}$$

The identical process would be used during the next cycle to calculate $\Delta\phi_{i+1}$ from $W_{i+1}$ and $W_i$ power measurements using $W_i$ from (76), $\widehat{\Delta\phi_i}$ from the (74) control law, (75) for the cubic term approximation, and their $W_{i+1}$, $\widehat{\Delta\phi_{i+1}}$ equivalents at $t_{i+1}$:

$$\begin{aligned} W_i &= 1 + \cos\left[\Delta\phi_i + \left(\Delta\varsigma_i - \Delta\varsigma_{i-1}\right) - \left(\Delta\xi_i - \Delta\xi_{i-1}\right)\right] \\ &= 1 + \cos\left(\Delta\phi_i - \Delta\phi_{i-1} - \pi/2 + 2\,n_i\,\pi\right) \\ W_{i+1} &= 1 + \cos\left[\Delta\phi_{i+1} + \left(\Delta\varsigma_{i+1} - \Delta\varsigma_i\right) - \left(\Delta\xi_{i+1} - \Delta\xi_i\right)\right] \\ &= 1 + \cos\left(\Delta\phi_{i+1} - \Delta\phi_i + \pi/2 + 2\,n_{i+1}\,\pi\right) \\ \Delta\phi_{i+1} &= \Delta\phi_{i-1} - \left(W_{i+1} - W_i\right) + \left(\Delta\phi_i - \Delta\phi_{i-1}\right)^3/3 \end{aligned} \tag{77}$$

Note the difference in polarity for $\left(W_{i+1} - W_i\right)$ in (77) compared with $\left(W_i - W_{i-1}\right)$ in (76). The variation is caused by the difference in $\pi/2$ term polarities in the (77) $W_i \to W_{i+1}$ sequence compared with the $W_{i-1} \to W_i$ sequence in (76). Thus, recursive computations for sequential $\Delta\phi$ determination must account for alternating signs on both the $\pi/2$ and $\left(W_i - W_{i-1}\right)$, $\left(W_{i+1} - W_i\right)$ terms in (76) and (77).

It remains to define settings for the $\Delta\varsigma$ s and $\Delta\xi$ s that satisfy (76) (and its next cycle (77) equivalent):

$$\begin{aligned}\left(\Delta\varsigma_{i-1}-\Delta\varsigma_{i-2}\right)-\left(\Delta\xi_{i-1}-\Delta\xi_{i-2}\right)&=-\Delta\phi_{i-2}+\pi/2+2\,n_{i-1}\pi\\ \left(\Delta\varsigma_{i}-\Delta\varsigma_{i-1}\right)-\left(\Delta\xi_{i}-\Delta\xi_{i-1}\right)&=-\Delta\phi_{i-1}-\pi/2+2\,n_{i}\pi\end{aligned} \tag{78}$$

A potential solution for the $\Delta\varsigma$ s and $\Delta\xi$ s in (78) might be to assign the alternating $\pi/2$ operations to the $\Delta\xi$ s, with the remaining $-\Delta\phi_{i-2}+2\,n_{i-1}\pi$ and $-\Delta\phi_{i-1}+2\,n_{i}\pi$ control operations assigned to the $\Delta\varsigma$ s. Another solution might be to set the $\Delta\xi$ s to zero (i.e., equating $\Delta\xi_{i}-\Delta\xi_{i-1}=0$ and $\Delta\xi_{i-1}-\Delta\xi_{i-2}=0$), and assign all operations in (78) to the $\Delta\varsigma$ s. In effect, this would represent a single L/N crystal biasing approach, implemented in Fig. 6 by maintaining the $\Delta\xi$ crystal presence (for component symmetry), but setting the $V_{\xi}$ voltage to zero. This would also allow a lower manufacturing cost option of eliminating the $\Delta\xi$ crystal entirely, i.e., an unsymmetrical single crystal approach. Appendix C discusses the single crystal approach in detail.

Another, but fully symmetric solution (and the one discussed for the remainder of this section), derives by first equating $n_i$ to $n_{\varsigma_i}+n_{\xi_i}$, and $n_{i-1}$ to $n_{\varsigma_{i-1}}+n_{\xi_{i-1}}$ where $n_{\varsigma_i}$, $n_{\xi_i}$, $n_{\varsigma_{i-1}}$, $n_{\xi_{i-1}}$ are integers. Thus, (78) becomes

$$\begin{aligned}\left(\Delta\varsigma_{i-1}-\Delta\varsigma_{i-2}\right)-\left(\Delta\xi_{i-1}-\Delta\xi_{i-2}\right)&=-\Delta\phi_{i-2}+\pi/2+2\left(n_{\varsigma_{i-1}}+n_{\xi_{i-1}}\right)\pi\\ \left(\Delta\varsigma_{i}-\Delta\varsigma_{i-1}\right)-\left(\Delta\xi_{i}-\Delta\xi_{i-1}\right)&=-\Delta\phi_{i-1}-\pi/2+2\left(n_{\varsigma_i}+n_{\xi_i}\right)\pi\end{aligned} \tag{79}$$

Dividing (79) into symmetrical $\Delta\varsigma$ and $\Delta\xi$ portions obtains

$$\begin{aligned}\left(\Delta\varsigma_{i-1}-\Delta\varsigma_{i-2}\right)&=-\Delta\phi_{i-2}/2+\pi/4+2\,n_{\varsigma_{i-1}}\pi\\ \left(\Delta\xi_{i-1}-\Delta\xi_{i-2}\right)&=\Delta\phi_{i-2}/2-\pi/4-2\,n_{\xi_{i-1}}\pi\\ \left(\Delta\varsigma_{i}-\Delta\varsigma_{i-1}\right)&=-\Delta\phi_{i-1}/2-\pi/4+2\,n_{\varsigma_i}\pi\\ \left(\Delta\xi_{i}-\Delta\xi_{i-1}\right)&=\Delta\phi_{i-1}/2+\pi/4-2\,n_{\varsigma_i}\pi\end{aligned} \tag{80}$$

Note that (79) equals the difference between the $\Delta\varsigma$ and $\Delta\xi$ expressions in (80). The recursive equivalent for the $\Delta\varsigma$ s and $\Delta\xi$ s in (80) then becomes

$$\begin{aligned}
\Delta\varsigma_{i-1} &= \Delta\varsigma_{i-2} - \Delta\phi_{i-2}/2 + \pi/4 + 2\,n_{\varsigma_{i-1}}\pi \\
\Delta\xi_{i-1} &= \Delta\xi_{i-2} + \Delta\phi_{i-2}/2 - \pi/4 - 2\,n_{\xi_{i-1}}\pi \\
\Delta\varsigma_{i} &= \Delta\varsigma_{i-1} - \Delta\phi_{i-1}/2 - \pi/4 + 2\,n_{\varsigma_{i}}\pi \\
\Delta\xi_{i} &= \Delta\xi_{i-1} + \Delta\phi_{i-1}/2 + \pi/4 - 2\,n_{\xi_{i}}\pi
\end{aligned} \tag{81}$$

Eqs. (81) with the $\Delta\theta$ output from (66) are the basis for the symmetric closed-loop FOG computations shown in Fig. 8. The $W^*_{i-1}$ and $W^*_i$ signals in Fig. 8 represent the A/D Converter outputs in Fig. 6 including the negative bias that is eliminated by the $W^*_i - W^*_{i-1}$ subtraction process, i.e.,

$$\begin{aligned}
W^*_{i-1} = W_{i-1} - W_{Bias} \qquad W^*_i = W_i - W_{Bias} \\
W^*_i - W^*_{i-1} = W_i - W_{i-1}
\end{aligned}. \tag{82}$$

where $W_{Bias}$ is the negative bias in Fig. 6 applied to the photo detector output. Then from (76) with (82),

$$\begin{aligned}
\Delta\phi_i &= \Delta\phi_{i-2} + (W_i - W_{i-1}) + (\Delta\phi_{i-1} - \Delta\phi_{i-2})^3/3 \\
&= \Delta\phi_{i-2} + \left(W^*_i - W^*_{i-1}\right) + (\Delta\phi_{i-1} - \Delta\phi_{i-2})^3/
\end{aligned} \tag{83}$$

which is used in Fig. 8 when calculating $\Delta\theta$ for output.

Saved From Past Cycle : $\Delta\phi_{i-1}$, $\Delta\phi_{i-2}$, $W^*_{i-1}$, $\Delta\varsigma_{i-1}$, $\Delta\xi_{i-1}$, $\delta\Delta\varsigma_{i-1}$, $\delta\Delta\xi_{i-1}$, $\delta\Delta\varsigma_{i-2}$, $\delta\Delta\xi_{i-2}$, $\Delta\Sigma_{i-1}$, $Sgn$

Start of Current Cycle

At $t_i$: Sample $W^*_i$

After $t_i$ But Before $t_{i+1}$:

Read $W^*_i$ From A/D Converter

Then Calculate :

$$Sgn = -Sgn$$

$$\Delta\varsigma_i = \Delta\varsigma_{i-1} - \Delta\phi_{i-1}/2 - Sgn\,\pi/4$$

$$DO\ Until\ \Delta\varsigma_i \le \Delta\beta_{OffSet} + 2\pi \quad IF\ \Delta\varsigma_i > \Delta\beta_{OffSet} + 2\pi\ \ Then\ \ \Delta\varsigma_i = \Delta\varsigma_i - 2\pi$$

$$DO\ Until\ \Delta\varsigma_i \ge \Delta\beta_{OffSet} \quad IF\ \Delta\varsigma_i < \Delta\beta_{OffSet}\ \ Then\ \ \Delta\varsigma_i = \Delta\varsigma_i + 2\pi$$

$$\Delta\xi_i = \Delta\xi_{i-1} + \Delta\phi_{i-1}/2 + Sgn\,\pi/4$$

$$DO\ Until\ \Delta\xi_i \le \Delta\beta_{OffSet} + 2\pi \quad IF\ \Delta\xi_i > \Delta\beta_{OffSet} + 2\pi\ \ Then\ \ \Delta\xi_i = \Delta\xi_i - 2\pi$$

$$DO\ Until\ \Delta\xi_i \ge \Delta\beta_{OffSet} \quad IF\ \Delta\xi_i < \Delta\beta_{OffSet}\ \ Then\ \ \Delta\xi_i = \Delta\xi_i + 2\pi$$

$$\widehat{\Delta\varsigma_i} = \mathrm{Round}\left(\Delta\varsigma_i\right) \qquad \widehat{\Delta\xi_i} = \mathrm{Round}\left(\Delta\xi_i\right)$$

$$\delta\Delta\varsigma_i = \widehat{\Delta\varsigma_i} - \Delta\varsigma_i \qquad \delta\Delta\xi_i = \widehat{\Delta\xi_i} - \Delta\xi_i$$

$$\Delta\phi_i = \Delta\phi_{i-2} + \left(\Delta\phi_{i-1} - \Delta\phi_{i-2}\right)^3/3 + Sgn\left(W^*_i - W^*_{i-1}\right) - \left(\delta\Delta\varsigma_i - \delta\Delta\varsigma_{i-2}\right) + \left(\delta\Delta\xi_i - \delta\Delta\xi_{i-2}\right)$$

$$\Delta\theta_i = \Delta\phi_i / k_{SF}$$

$$\Sigma_i = \Delta\Sigma_{i-1} + \Delta\theta_i$$

$$\widehat{\Delta\theta_i} = \mathrm{Round}\left(\Sigma_i\right)$$

$$\Delta\Sigma_i = \Sigma_i - \widehat{\Delta\theta_i}$$

Output: $\widehat{\Delta\theta_i}$ As Digital Word To User

Output: $\widehat{\Delta\varsigma_i}$, $\widehat{\Delta\xi_i}$ Through D/A Converter And Apply To L/N Crystals

Save For Next Cycle : $\Delta\phi_i$, $\Delta\phi_{i-1}$, $W^*_i$, $\Delta\varsigma_i$, $\Delta\xi_i$, $\delta\Delta\varsigma_i$, $\delta\Delta\xi_i$, $\delta\Delta\varsigma_{i-1}$, $\delta\Delta\xi_{i-1}$, $\Delta\Sigma_i$, $Sgn$

Repeat For Next Cycle

Fig. 8 – Dual Crystal Closed-Loop FOG Symmetrical Computation Flow

The *Sgn* term in Fig. 8 accounts for alternating polarities in $\pi / 2$ and $(W_i - W_{i-1})$ of (76) compared with the next cycle equivalents in (77). The $2\, n_\varsigma\, \pi$, $2\, n_\xi\, \pi$ terms in (81) are used to assure that $\Delta\varsigma$, $\Delta\xi$ values applied to the lithium-niobate (L/N) crystals in Fig. 6 remain positive (greater than $\Delta\beta_{OffSet}$) and within a specified range for proper operation. This is achieved by logic statements in Fig. 8 that apply successive plus or minus $2\pi$ changes to $\Delta\varsigma$, $\Delta\xi$ until they satisfy the specified criteria.

The *Sgn* term in the $\Delta\varsigma_i$, $\Delta\xi_i$ computations of Fig. 8 accounts for alternating polarities in $\pi / 4$ compared with next cycle equivalents in (81). The *Sgn* term is also used in the $\Delta\phi_i$ computation of Fig. 8 to account for alternating polarities in $(W_i - W_{i-1})$ compared with next cycle equivalents in (76) and (77). The $2\, n_\varsigma\, \pi$, $2\, n_\xi\, \pi$ terms in (81) are used to assure that $\Delta\varsigma$, $\Delta\xi$ values applied to the lithium-niobate (L/N) crystals in Fig. 6 remain positive (greater than $\Delta\beta_{OffSet}$) and within a specified range for proper operation. This is achieved by logic statements in Fig. 8 that apply successive plus or minus $2\pi$ changes to $\Delta\varsigma$, $\Delta\xi$ until they satisfy the specified criteria.

The DA/Round operations in Fig. 8 round the computed $\Delta\varsigma$, $\Delta\xi$ values to $\widehat{\Delta\varsigma}$, $\widehat{\Delta\xi}$ at the same bit level as the Fig. 6 D/A converters, thereby eliminating round-off error that would occur in the D/A conversion process if $\Delta\varsigma$, $\Delta\xi$ were applied as computed (with uncertain round-off error then imposed on the L/N crystals in the D/A conversion process). Having $\left(W_i^* - W_{i-1}^*\right)$ in Fig. 8 computed based on applying rounded $\widehat{\Delta\varsigma}$, $\widehat{\Delta\xi}$ to the crystals would create error in calculating $\Delta\phi_i$ and the resulting $\Delta\theta_i$ output. However, the $\widehat{\Delta\varsigma}$, $\widehat{\Delta\xi}$ error is known (calculated as $\delta\Delta\varsigma$ and $\delta\Delta\xi$ in Fig. 8), hence, eliminated in Fig. 8 by correcting the $\left(W_i^* - W_{i-1}^*\right)$ value used in the $\Delta\phi_i$ calculation. A derivation of the $\delta\Delta\varsigma$ and $\delta\Delta\xi$ correction process is provided in Appendix B.

Additional round-off error can be generated when digitally outputting $\Delta\theta_i$ due to limited word length in the D/D (Digital-to-Digital) conversion function. This error is eliminated using the D/D Round function in Fig. 8, by computing $\widehat{\Delta\theta}$ (a rounded version of $\Delta\theta$), for output at the D/D function word length. The $\widehat{\Delta\theta}$ output is designed in Fig. 8 to assure that the sum of transmitted rounded $\widehat{\Delta\theta}$s equals the sum of the correct $\Delta\theta$s by cyclically controlling their summed difference $\Delta\Sigma$ to remain small. The result is a bounded error on the sum (integral) of the $\widehat{\Delta\theta}$s that varies randomly at the magnitude of the lowest bit level in $\widehat{\Delta\theta}$.

Finally, we address the round-off error generated in Fig. 8 when reading the $W_{i-1}^*$ and $W_i^*$ measurements through the A/D Converter in Fig. 6. This error is minimized by setting the

analog negative bias signal in Fig. 6 to correspond to the expected unity value of the normalized photo detector $W_i$ power measurement under closed-loop control. The result is an A/D converter input signal that is nominally zero, being only offset by the uncertainty in the photo detector output, the error in the analog bias, and the small dynamic lag in closed loop control operations. This enables scaling of the A/D converter so that the magnitude of the least significant bit (the effective round-off error) becomes negligible in the Fig. 8 calculations.

## CONCLUSIONS

Optical gyros generate oppositely directed monochromatic light waves travelling in a closed-circuit waveguide to measure angular rotation relative to non-rotating inertial space. Based on classical Galilean/Newtonian kinematics and Relativity theory (under normal operating conditions), the wavelength of light waves in the waveguide will change due to angular rotation, increasing for waves travelling with rotation, decreasing for waves travelling against rotation. Due to Relativity theory, the velocity of the waves will remain constant (at the speed of light) relative to any point on the waveguide. As a result, relative to the readout device in the waveguide, the frequency will decrease for waves travelling with rotation, and increase for waves travelling against rotation. Additionally, relative to any point on the waveguide during rotation, the time increment for a wave to traverse a given distance increment will be the same, independent of its motion relative to the rotation direction. A corollary is that relative to the waveguide, the time interval for a wave to traverse a given distance will be the same for waves travelling in either direction.

Ring laser gyros (RLGs) and fiber optic gyros (FOGs) are integrating angular rate sensing inertial instruments, both measuring increments of gyro angular rotation relative to non-rotating inertial space. The analytics describing RLG and FOG operations emanate from the same fundamental equation. RLGs and FOGs differ analytically in the method used to extract incremental angular data measurements for output. Application of the fundamental equation for each depends on the total travel time for a light wave to traverse the waveguide.

Due to the stimulated-emission process, a light wave in an RLG will continue to traverse the waveguide from gyro turn-on. The result is a pair of continuous counter-travelling light waves that combine at the readout, generating an optical interference pattern across the readout zone. The interference pattern moves across readout photo detectors at a rate proportional to the frequency difference between the counter-travelling light waves. The frequency difference is proportional to angular rate. The RLG output measures the occurrence of each interference pattern traversal, each representing a known increment of angular rotation relative to non-rotating inertial space.

In contrast, each light wave in a FOG only traverses the waveguide once from the time it leaves the FOG photo diode light source until it arrives at the readout photo detector. In a FOG, rotation generates a phase difference at the readout between the counter-travelling light waves. The phase difference is proportional to the increment of angular rotation during the time for a wave to traverse the waveguide. When the counter-travelling waves combine at the readout, the phase difference generates a change in the combined wave optical power illuminating the photo

detector. Suitable closed-loop electronics convert photo detector optical power measurements into angular increments for output, while generating commands to lithium-niobate biasing crystal inserts in the gyro wave path for closed-loop control.

## APPENDIX A

## DERIVATION OF EQ. (12) USING RELATIVITY THEORY

The equivalent to (12) based on Relativity theory [4 Eq (12-5a); 5 Eq (10.31)-(10.32)] in its equivalent point-to-point differential form [3 Eq (35)] is:

$$d\underline{x}_{p/b} = d\underline{x}_{p/a} - \underline{v}_{b/a}\, dt_a + \left( \frac{1}{\sqrt{1 - v_{ab}^2 / c^2}} - 1 \right) \left( d\underline{x}_{p/a} \cdot \underline{v}_{b/a}\, \underline{v}_{b/a} / v_{ab}^2 - \underline{v}_{b/a}\, dt_a \right) \qquad \text{(A-1)}$$

where $\underline{v}_{b/a}$ is the instantaneous velocity of point *b* observed at point *a*, $v_{ab}$ is the magnitude of $\underline{v}_{b/a}$, and $dt_a$ is the differential time interval for the $d\underline{x}_{p/b}$ and $d\underline{x}_{p/a}$ differential position changes that would be measured on a clock located at point *a*. The peculiar $\sqrt{1 - v_{ab}^2 / c^2}$ term in (A-1) is a unique contribution from Relativity theory [3; 6 Appndx A] that assures that if point *p* is travelling at the speed of light *c*, the magnitude of *p* velocity relative to observation points *a* or *b* will be the same *c* constant:

$$\begin{aligned} \left| d\underline{x}_{p/a} / dt_a \right| &= \sqrt{\left( d\underline{x}_{p/a} / dt_{p_a} \right) \cdot \left( d\underline{x}_{p/a} / dt_a \right)} \\ = \left| d\underline{x}_{p/b} / dt_b \right| &= \sqrt{\left( d\underline{x}_{p/b} / dt_b \right) \cdot \left( d\underline{x}_{p/b} / dt_b \right)} = c \end{aligned} \qquad \text{(A-2)}$$

where $dt_b$ is the time interval for the $d\underline{x}_{p/b}$ and $d\underline{x}_{p/a}$ differential motion that would be measured on a clock located at point *b*. Eq. (A-1) is also based on $\underline{v}_{a/b}$, the velocity of point *a* observed at point *b*, being of equal magnitude but oppositely directed from $\underline{v}_{b/a}$ (the velocity of point *b* observed at point *a*), a fundamental premise of both classical Newtonian kinematics and Relativity theory [2 pp 236-238; 5 pp 30],

$$\underline{v}_{b/a} \equiv \frac{d\underline{x}_{b/a}}{dt_a} \qquad \underline{v}_{a/b} \equiv \frac{d\underline{x}_{a/b}}{dt_b} \qquad \underline{v}_{a/b} = -\underline{v}_{b/a} \qquad v_{ab} \equiv \left| \underline{v}_{b/a} \right| = \left| \underline{v}_{a/b} \right| \qquad \text{(A-3)}$$

For the commonly encountered situations when $v_{ab} \ll c$, the $\sqrt{1 - v_{ab}^2 / c^2}$ Relativity coefficient in (A-1) approximates as unity and (A-1) simplifies to

$$d\underline{x}_{p/b} = d\underline{x}_{p/a} - \underline{v}_{b/a}\, dt_{p_a} \qquad \text{(A-4)}$$

Substituting $\underline{v}_{b/a}\,dt_a = d\underline{x}_{b/a}$ from (A-3) into (A-4) obtains (12) in the main text, derived using classical Galilean/Newtonian kinematic theory:

$$d\underline{x}_{p/b} = d\underline{x}_{p/a} - d\underline{x}_{b/a} \tag{A-5}$$

## APPENDIX B

## DERIVING ROUND-OFF ERROR CORRECTIONS TO FOG LITHIUM-NIOBATE CRYSTAL COMMAND VOLTAGES

This appendix derives the $\Delta\phi_i$ equation in Fig. 8 used to correct the error generated by using rounded $\widehat{\Delta\varsigma}$, $\widehat{\Delta\xi}$ data for biasing the L/N crystals in Fig. 6. The derivation begins with definitions for $\widehat{\Delta\varsigma}$, $\widehat{\Delta\xi}$ in terms of non-rounded $\Delta\varsigma$, $\Delta\xi$ and the $\delta\Delta\varsigma$, $\delta\Delta\xi$ round-off errors in Fig. 8:

$$\begin{aligned}
\widehat{\Delta\varsigma_{i-1}} &= \Delta\varsigma_{i-1} + \delta\Delta\varsigma_{i-1} \qquad \widehat{\Delta\varsigma_{i-2}} = \Delta\varsigma_{i-2} + \delta\Delta\varsigma_{i-2} \\
\widehat{\Delta\xi_{i-1}} &= \Delta\xi_{i-1} + \delta\Delta\xi_{i-1} \qquad \widehat{\Delta\xi_{i-2}} = \Delta\xi_{i-2} + \delta\Delta\xi_{i-2} \\
\widehat{\Delta\varsigma_{i}} &= \Delta\varsigma_{i} + \delta\Delta\varsigma_{i} \qquad \widehat{\Delta\varsigma_{i-1}} = \Delta\varsigma_{i-1} + \delta\Delta\varsigma_{i-1} \\
\widehat{\Delta\xi_{i}} &= \Delta\xi_{i} + \delta\Delta\xi_{i} \qquad \widehat{\Delta\xi_{i-1}} = \Delta\xi_{i-1} + \delta\Delta\xi_{i-1}
\end{aligned} \tag{B-1}$$

Use of rounded L/N input produces combined power values $W$ having the same form as (67) – (68), but with $\Delta\varsigma$, $\Delta\xi$ replaced by $\widehat{\Delta\varsigma}$, $\widehat{\Delta\xi}$:

$$\begin{aligned}
W_{i-1} &= 1 + \cos\left[\Delta\phi_{i-1} + \left(\widehat{\Delta\varsigma_{i-1}} - \widehat{\Delta\varsigma_{i-2}}\right) - \left(\widehat{\Delta\xi_{i-1}} - \widehat{\Delta\xi_{i-2}}\right)\right] \\
W_{i} &= 1 + \cos\left[\Delta\phi_{i} + \left(\widehat{\Delta\varsigma_{i}} - \widehat{\Delta\varsigma_{i-1}}\right) - \left(\widehat{\Delta\xi_{i}} - \widehat{\Delta\xi_{i-1}}\right)\right]
\end{aligned} \tag{B-2}$$

Substituting (B-1) into (B-2) obtains

$$
\begin{aligned}
W_{i-1} &= 1+\cos\left[\Delta\phi_{i-1}+\left(\widehat{\Delta\varsigma_{i-1}}-\widehat{\Delta\varsigma_{i-2}}\right)-\left(\widehat{\Delta\xi_{i-1}}-\widehat{\Delta\xi_{i-2}}\right)\right] \\
&= 1+\cos\left\{\begin{array}{c}\Delta\phi_{i-1}+\left[\left(\Delta\varsigma_{i-1}+\delta\Delta\varsigma_{i-1}\right)-\left(\Delta\varsigma_{i-2}+\delta\Delta\varsigma_{i-2}\right)\right] \\ -\left[\left(\Delta\xi_{i-1}+\delta\Delta\xi_{i-1}\right)-\left(\Delta\xi_{i-2}+\delta\Delta\xi_{i-2}\right)\right]\end{array}\right\} \\
&= 1+\cos\left[\begin{array}{c}\Delta\phi_{i-1}+\left(\Delta\varsigma_{i-1}-\Delta\varsigma_{i-2}\right)-\left(\Delta\xi_{i-1}-\Delta\xi_{i-2}\right) \\ +\left(\delta\Delta\varsigma_{i-1}-\delta\Delta\varsigma_{i-2}\right)-\left(\delta\Delta\xi_{i-1}-\delta\Delta\xi_{i-2}\right)\end{array}\right]
\end{aligned}
\tag{B-3}
$$

$$
\begin{aligned}
W_i &= 1+\cos\left[\Delta\phi_i+\left(\widehat{\Delta\varsigma_i}-\widehat{\Delta\varsigma_{i-1}}\right)-\left(\widehat{\Delta\xi_i}-\widehat{\Delta\xi_{i-1}}\right)\right] \\
&= 1+\cos\left\{\Delta\phi_i+\left[\left(\Delta\varsigma_i+\delta\Delta\varsigma_i\right)-\left(\Delta\varsigma_{i-1}+\delta\Delta\varsigma_{i-1}\right)\right]-\left[\left(\Delta\xi_i+\delta\Delta\xi_i\right)-\left(\Delta\xi_{i-1}+\delta\Delta\xi_{i-1}\right)\right]\right\} \\
&= 1+\cos\left[\Delta\phi_i+\left(\Delta\varsigma_i-\Delta\varsigma_{i-1}\right)-\left(\Delta\xi_i-\Delta\xi_{i-1}\right)+\left(\delta\Delta\varsigma_i-\delta\Delta\varsigma_{i-1}\right)-\left(\delta\Delta\xi_i-\delta\Delta\xi_{i-1}\right)\right]
\end{aligned}
$$

The unrounded $\left(\Delta\varsigma_{i-1}-\Delta\varsigma_{i-2}\right)$, $\left(\Delta\xi_{i-1}-\Delta\xi_{i-2}\right)$, $\left(\Delta\varsigma_i-\Delta\varsigma_{i-1}\right)$, $\left(\Delta\xi_i-\Delta\xi_{i-1}\right)$ terms in (B-3) are from (81):

$$
\begin{aligned}
\left(\Delta\varsigma_{i-1}-\Delta\varsigma_{i-2}\right) &= -\Delta\phi_{i-2}/2+\pi/4+2\,n_{\varsigma_{i-1}}\pi \\
\left(\Delta\xi_{i-1}-\Delta\xi_{i-2}\right) &= \Delta\phi_{i-2}/2-\pi/4-2\,n_{\xi_{i-1}}\pi \\
\left(\Delta\varsigma_i-\Delta\varsigma_{i-1}\right) &= -\Delta\phi_{i-1}/2-\pi/4+2\,n_{\varsigma_i}\pi \\
\left(\Delta\xi_i-\Delta\xi_{i-1}\right) &= \Delta\phi_{i-1}/2+\pi/4-2\,n_{\xi_i}\pi
\end{aligned}
\tag{B-4}
$$

Substituting (B-4) into (B-3) then gives

$$
\begin{aligned}
W_{i-1} &= 1+\cos\left[\begin{array}{c}\Delta\phi_{i-1}-\Delta\phi_{i-2}+\pi/2+2\left(n_{\varsigma_{i-1}}+n_{\xi_{i-1}}\right)\pi \\ +\left(\delta\Delta\varsigma_{i-1}-\delta\Delta\varsigma_{i-2}\right)-\left(\delta\Delta\xi_{i-1}-\delta\Delta\xi_{i-2}\right)\end{array}\right] \\
&= 1-\sin\left[\Delta\phi_{i-1}-\Delta\phi_{i-2}+\left(\delta\Delta\varsigma_{i-1}-\delta\Delta\varsigma_{i-2}\right)-\left(\delta\Delta\xi_{i-1}-\delta\Delta\xi_{i-2}\right)\right] \\
&\approx 1-\left[\Delta\phi_{i-1}-\Delta\phi_{i-2}+\left(\delta\Delta\varsigma_{i-1}-\delta\Delta\varsigma_{i-2}\right)-\left(\delta\Delta\xi_{i-1}-\delta\Delta\xi_{i-2}\right)\right]
\end{aligned}
\tag{B-5}
$$

$$
\begin{aligned}
W_i &= 1+\cos\left[\Delta\phi_i-\Delta\phi_{i-1}-\pi/2+2\left(n_{\varsigma_i}+n_{\xi_i}\right)\pi+\left(\delta\Delta\varsigma_i-\delta\Delta\varsigma_{i-1}\right)-\left(\delta\Delta\xi_i-\delta\Delta\xi_{i-1}\right)\right] \\
&= 1+\sin\left[\Delta\phi_i-\Delta\phi_{i-1}+\left(\delta\Delta\varsigma_i-\delta\Delta\varsigma_{i-1}\right)-\left(\delta\Delta\xi_i-\delta\Delta\xi_{i-1}\right)\right] \\
&\approx 1+\Delta\phi_i-\Delta\phi_{i-1}+\left(\delta\Delta\varsigma_i-\delta\Delta\varsigma_{i-1}\right)-\left(\delta\Delta\xi_i-\delta\Delta\xi_{i-1}\right)
\end{aligned}
$$

Subtracting $W_{i-1}$ from $W_i$ in (B-5) obtains

$$\begin{aligned} W_i - W_{i-1} &= \Delta\phi_i - \Delta\phi_{i-1} + \left(\delta\Delta\varsigma_i - \delta\Delta\varsigma_{i-1}\right) - \left(\delta\Delta\xi_i - \delta\Delta\xi_{i-1}\right) \\ &+ \Delta\phi_{i-1} - \Delta\phi_{i-2} + \left(\delta\Delta\varsigma_{i-1} - \delta\Delta\varsigma_{i-2}\right) - \left(\delta\Delta\xi_{i-1} - \delta\Delta\xi_{i-2}\right) \\ &= \Delta\phi_i - \Delta\phi_{i-2} + \left(\delta\Delta\varsigma_i - \delta\Delta\varsigma_{i-2}\right) - \left(\delta\Delta\xi_i - \delta\Delta\xi_{i-2}\right) \end{aligned} \tag{B-6}$$

from which

$$\Delta\phi_i = \Delta\phi_{i-2} + \left(W_i - W_{i-1}\right) - \left(\delta\Delta\varsigma_i - \delta\Delta\varsigma_{i-2}\right) + \left(\delta\Delta\xi_i - \delta\Delta\xi_{i-2}\right) \tag{B-7}$$

The identical procedure for the next cycle finds

$$\widehat{\Delta\varsigma_{i+1}} = \Delta\varsigma_{i+1} + \delta\Delta\varsigma_{i+1} \qquad \widehat{\Delta\varsigma_i} = \Delta\varsigma_i + \delta\Delta\varsigma_i$$
$$\widehat{\Delta\xi_{i+1}} = \Delta\xi_{i+1} + \delta\Delta\xi_{i+1} \qquad \widehat{\Delta\xi_i} = \Delta\xi_i + \delta\Delta\xi_i$$

$$\begin{aligned} W_{i+1} &= 1 + \cos\left[\Delta\phi_{i+1} + \left(\widehat{\Delta\varsigma_{i+1}} - \widehat{\Delta\varsigma_i}\right) - \left(\widehat{\Delta\xi_{i+1}} - \widehat{\Delta\xi_i}\right)\right] \\ &= 1 + \cos\left[\Delta\phi_{i+1} + \left(\Delta\varsigma_{i+1} - \Delta\varsigma_i\right) - \left(\Delta\xi_{i+1} - \Delta\xi_i\right) + \left(\delta\Delta\varsigma_{i+1} - \delta\Delta\varsigma_i\right) - \left(\delta\Delta\xi_{i+1} - \delta\Delta\xi_i\right)\right] \end{aligned} \tag{B-8}$$

$$\left(\Delta\varsigma_{i+1} - \Delta\varsigma_i\right) = -\Delta\phi_i / 2 + \pi / 4 + 2\, n_{\varsigma_{i+1}}\pi$$
$$\left(\Delta\xi_{i+1} - \Delta\xi_i\right) = \Delta\phi_i / 2 - \pi / 4 - 2\, n_{\xi_{i+1}}\pi$$

$$\begin{aligned} W_{i+1} &= 1 + \cos\left[\Delta\phi_{i+1} - \Delta\phi_i + \pi / 2 + 2\left(n_{\varsigma_{i+1}} + n_{\xi_{i+1}}\right)\pi + \left(\delta\Delta\varsigma_{i+1} - \delta\Delta\varsigma_i\right) - \left(\delta\Delta\xi_{i+1} - \delta\Delta\xi_i\right)\right] \\ &= 1 - \sin\left[\Delta\phi_{i+1} - \Delta\phi_i + \left(\delta\Delta\varsigma_{i+1} - \delta\Delta\varsigma_i\right) - \left(\delta\Delta\xi_{i+1} - \delta\Delta\xi_i\right)\right] \\ &\approx 1 - \left(\Delta\phi_{i+1} - \Delta\phi_i\right) - \left(\delta\Delta\varsigma_{i+1} - \delta\Delta\varsigma_i\right) + \left(\delta\Delta\xi_{i+1} - \delta\Delta\xi_i\right) \end{aligned}$$

Subtracting $W_i$ in (B-5) from $W_{i+1}$ in (B-8) obtains

$$\begin{aligned} W_{i+1} - W_i &= -\left(\Delta\phi_{i+1} - \Delta\phi_i\right) - \left(\delta\Delta\varsigma_{i+1} - \delta\Delta\varsigma_i\right) + \left(\delta\Delta\xi_{i+1} - \delta\Delta\xi_i\right) \\ &- \left[\Delta\phi_i - \Delta\phi_{i-1} + \left(\delta\Delta\varsigma_i - \delta\Delta\varsigma_{i-1}\right) - \left(\delta\Delta\xi_i - \delta\Delta\xi_{i-1}\right)\right] \\ &= -\Delta\phi_{i+1} + \Delta\phi_{i-1} - \left(\delta\Delta\varsigma_{i+1} - \delta\Delta\varsigma_{i-1}\right) + \left(\delta\Delta\xi_{i+1} - \delta\Delta\xi_{i-1}\right) \end{aligned} \tag{B-9}$$

from which,

$$\Delta\phi_{i+1} = \Delta\phi_{i-1} - (W_{i+1} - W_i) - (\delta\Delta\varsigma_{i+1} - \delta\Delta\varsigma_{i-1}) + (\delta\Delta\xi_{i+1} - \delta\Delta\xi_{i-1}) \quad \text{(B-10)}$$

Thus, for two successive cycles, (B-7) and (B-10) show that

$$\begin{aligned} \Delta\phi_i &= \Delta\phi_{i-2} + (W_i - W_{i-1}) - (\delta\Delta\varsigma_i - \delta\Delta\varsigma_{i-2}) + (\delta\Delta\xi_i - \delta\Delta\xi_{i-2}) \\ \Delta\phi_{i+1} &= \Delta\phi_{i-1} - (W_{i+1} - W_i) - (\delta\Delta\varsigma_{i+1} - \delta\Delta\varsigma_{i-1}) + (\delta\Delta\xi_{i+1} - \delta\Delta\xi_{i-1}) \end{aligned} \quad \text{(B-11)}$$

The (B-11) expressions are identical except for the difference in polarity for the $W$ power difference term in $\Delta\phi_{i+1}$ compared with its equivalent in $\Delta\phi_i$. A common formula for both can be defined as

$$\Delta\phi_i = \Delta\phi_{i-2} + Sgn(W_i - W_{i-1}) - (\delta\Delta\varsigma_i - \delta\Delta\varsigma_{i-2}) + (\delta\Delta\xi_i - \delta\Delta\xi_{i-2}) \quad \text{(B-12)}$$

where *Sgn* is unity in magnitude and alternating in polarity from $i$ cycle to $i$ cycle. Eq. (B-12) is what is shown in Fig. 8 with from (B-1):

$$\begin{aligned} \delta\Delta\varsigma_{i-1} &= \widehat{\Delta\varsigma_{i-1}} - \Delta\varsigma_{i-1} \quad & \delta\Delta\varsigma_{i-2} &= \widehat{\Delta\varsigma_{i-2}} - \Delta\varsigma_{i-2} \\ \delta\Delta\xi_{i-1} &= \widehat{\Delta\xi_{i-1}} - \Delta\xi_{i-1} \quad & \delta\Delta\xi_{i-2} &= \widehat{\Delta\xi_{i-2}} - \Delta\xi_{i-2} \end{aligned} \quad \text{(B-13)}$$

## APPENDIX C

## SINGLE CRYSTAL CLOSED LOOP CONTROL

A single lithium-niobate crystal biasing approach can be used for closed-loop FOG operations by setting the $\Delta\xi$ s in Fig. 6 to zero so that the recursive form of (79) becomes

$$\begin{aligned} \Delta\varsigma_{i-1} &= \Delta\varsigma_{i-2} - \Delta\phi_{i-2} + \pi/2 + 2\,n_{\varsigma_{i-1}}\pi \\ \Delta\varsigma_i &= \Delta\varsigma_{i-1} - \Delta\phi_{i-1} - \pi/2 + 2\,n_{\varsigma_i}\pi \end{aligned} \quad \text{(C-1)}$$

Eqs. (C-1) with (83) for $\Delta\phi_i$ and $\Delta\theta$ output from (66), are the basis for the single crystal closed-loop FOG computation operations shown in Fig. 9.

Saved From Past Cycle : $\Delta\phi_{i-1}, \Delta\phi_{i-2}, W^*_{i-1}, \Delta\varsigma_{i-1}, \delta\Delta\varsigma_{i-1}, \delta\Delta\varsigma_{i-2}, \Delta\Sigma_{i-1}, Sgn$

Start of Current Cycle

At $t_i$ : Sample $W^*_i$

After $t_i$ But Before $t_{i+1}$ :

Read $W^*_i$ From A/D Converter

Then Calculate :

$$Sgn = -Sgn$$

$$\Delta\varsigma_i = \Delta\varsigma_{i-1} - \Delta\phi_{i-1} - Sgn\ \pi/2$$

$$DO\ Until\ \Delta\varsigma_i \le \Delta\beta_{OffSet} + 2\pi \quad IF\ \Delta\varsigma_i > \Delta\beta_{OffSet} + 2\pi\ \ Then\ \ \Delta\varsigma_i = \Delta\varsigma_i - 2\pi$$

$$DO\ Until\ \Delta\varsigma_i \ge \Delta\beta_{OffSet} \quad IF\ \Delta\varsigma_i < \Delta\beta_{OffSet}\ \ Then\ \ \Delta\varsigma_i = \Delta\varsigma_i + 2\pi$$

$$\widehat{\Delta\varsigma_i} = \text{Round}\left(\Delta\varsigma_i\right)$$

$$\delta\Delta\varsigma_i = \widehat{\Delta\varsigma_i} - \Delta\varsigma_i$$

$$\Delta\phi_i = \Delta\phi_{i-2} + \left(\Delta\phi_{i-1} - \Delta\phi_{i-2}\right)^3/3 + Sgn\left(W^*_i - W^*_{i-1}\right) - \left(\delta\Delta\varsigma_i - \delta\Delta\varsigma_{i-2}\right)$$

$$\Delta\theta_i = \Delta\phi_i / k_{SF}$$

$$\Sigma_i = \Delta\Sigma_{i-1} + \Delta\theta_i$$

$$\widehat{\Delta\theta_i} = \text{Round}\left(\Sigma_i\right)$$

$$\Delta\Sigma_i = \Sigma_i - \widehat{\Delta\theta_i}$$

Output: $\widehat{\Delta\theta_i}$ As Digital Word To User

Output: $\widehat{\Delta\varsigma_i}$ Through D/A Converter And Apply To L/N Crystal

Save For Next Cycle : $\Delta\phi_i, \Delta\phi_{i-1}, W^*_i, \Delta\varsigma_i, \delta\Delta\varsigma_i, \delta\Delta\varsigma_{i-1}, \Delta\Sigma_i, Sgn$

Repeat For Next Cycle

Fig. 9 – Single Crystal Closed-Loop FOG Computation Flow

In Fig. 9, the $W^*_{i-1}$ and $W^*_i$ signals represent the A/D Converter output in Fig. 6 including the negative bias applied to the photo detector output. The $Sgn$ term in Fig. 9 accounts for $\pi/2$

and $(W_i - W_{i-1})$ alternating polarities in (76) compared with their next cycle equivalents in (77). The $2\, n_\varsigma\, \pi$ term in (C-1) is used to assure that the $\Delta\varsigma$ value applied to the lithium-niobate (L/N) cell in Fig. 6 remains positive (greater than $\Delta\beta_{OffSet}$) and within a specified range for proper operation. This is achieved by logic statements in Fig. 9 that apply successive plus or minus $2\pi$ changes to $\Delta\varsigma$ until it satisfies the specified criteria.

The DA/Round operations in Fig. 9 round the computed $\Delta\varsigma$ values to $\widehat{\Delta\varsigma}$ for output at the same bit level as the Fig. 6 $\Delta\varsigma$ D/A converter, thereby eliminating round-off error that would occur in the D/A conversion process if $\Delta\varsigma$ were applied as computed (with uncertain round-off error then imposed on the L/N crystals in the D/A conversion process). Having $W_i^* - W_{i-1}^*$ in Fig. 9 computed based on applying rounded $\widehat{\Delta\varsigma}$ to the crystal would create error in calculating $\Delta\phi_i$ and the resulting $\Delta\theta_i$ output. However, the $\widehat{\Delta\varsigma}$ error is known (calculated as $\delta\Delta\varsigma$ in Fig. 9), thus, eliminated in Fig. 9 by correcting the $\left(W_i^* - W_{i-1}^*\right)$ value used in the $\Delta\phi_i$ calculation. A derivation of the $\delta\Delta\varsigma$ correction process is provided in Appendix B.

Additional round-off error can be generated when digitally outputting $\Delta\theta_i$ due to limited word length in the D/D (Digital-to-Digital) conversion function. This error is eliminated using the D/D Round function in Fig. 9, by generating $\widehat{\Delta\theta}$ (a rounded version of $\Delta\theta$), for output at the D/D function word length. The $\widehat{\Delta\theta}$ output is designed in Fig. 9 to assure that the sum of transmitted rounded $\widehat{\Delta\theta}$s equals the sum of the correct $\Delta\theta$s by cyclically controlling their summed difference $\Delta\Sigma$ to remain small. The result is a bounded error on the sum (integral) of the $\widehat{\Delta\theta}$s that varies randomly at the magnitude of the lowest bit level in $\widehat{\Delta\theta}$.

Finally, we address the round-off error generated in Fig. 9 when reading the $W_{i-1}^*$ and $W_i^*$ measurements through the A/D Converter in Fig. 6. This error is minimized by setting the analog negative bias signal in Fig. 6 to correspond to the expected unity value of the normalized photo detector $W_i$ power measurement under closed-loop control. The result is an A/D converter input signal that is nominally zero, being only offset by the uncertainty in the photo detector output, the error in the analog bias, and the small dynamic lag in closed loop control operations. This enables scaling of the A/D converter so that the magnitude of the least significant bit (the effective round-off error) becomes negligible in the Fig. 9 calculations.

REFERENCES

[1] Einstein, A., *Relativity, The Special and the General Theory*, 1961, The Estate of Albert Einstein.

[2] Born, Max, *Einstein's Theory of Relativity*, Dover Publications, Inc., New York

[3] Savage, P. G., "Differential Kinematics Of Point-To-Point Relativity", SAI WBN-14021, March 11, 2018, free access available at www.strapdownassociates.com.

[4] Halfman, Robert L., *Dynamics: Systems, Variational Methods, Relativity, Volume II*, Addison-Wesley, 1962.

[5] Fock, V., *Theory of Space, Time, and Gravitation, Second Revised Edition*, New York: Pergamon Press, 1964

[6] Savage, P. G., "Differential Point-To-Point Relativity In Rotating Coordinates", SAI WBN-14022, May 28, 2018, free access available at www.strapdownassociates.com.

[7] Savage, P. G., *Strapdown Analytics, Edition II*, Strapdown Associates, Inc., 2007

[8] Savage, P. G., "Introduction To The Kinematics Of Point-To-Point Relativity", WBN-14015, Strapdown Associates, Inc., April 17, 2016 (Updated January 29, 2018), free access available at www.strapdownassociates.com.

[9] Sokolnikoff, I. S. & Redheffer, R. M.; *Mathematics of Physics and Modern Engineering*, McGraw-Hill, New York, London, Toronto, 1958.

[10] Killpatrick, Joseph, "The Laser Gyro", IEEE Spectrum, Oct. 1967.

[11] Aronowitz, F., "Fundamentals of the Ring Laser Gyro", Paper 3., *Optical Gyros And their Applications*, NATO RTO-AG-339, May 1999.

[12] Smith, I. and Dorschner, T., "Clear-Path Four-Frequency Ring Laser Gyroscope", Journal of the Optical Society of America, Volume 68, pp. 1381, 1978.

[13] Lawrence, A., *Modern Inertial Technology*, Springer-Verlag 1993.

[14] Lefevre, C. L.., "Application Of The Sagnac Effect In The Interferometric Fiber-Optic Gyroscope", Paper 7., *Optical Gyros And their Applications*, NATO RTO-AG-339, May 1999.

[15] Ezekiel, S. and Arditty, H.J., ed. *Fiber Optic Rotation Sensors and Related Technologies*, Springer-Verlag, Berlin/Heidelberg/New York, 1982.

[16] Savage, P.G., "Blazing Gyros – The Evolution of Strapdown Inertial Navigation Technology For Aircraft", *AIAA Journal Of Guidance, Control, And Dynamics*, Vol. 36, No. 3, May - June, 2013, pp. 637-655, also posted for free-access as WBN-14009 at www.strapdownassociates.com.